Highlights

- Firn area of studied glaciers between 2012 and 2017 decreased from 24% to 41%
- Max. loss of 14% of firn contribution to glacier area was recorded on Hansbreen
- Hornsund's local climatic conditions shape east-to-west gradient of firn area loss
- The Internal Reflection Power is recommended for glacier zones distinction by GPR
- Results of analysis of modern SAR data are promising for distinguishing firn and SI

Changes of Glacier Facies on Hornsund Glaciers (Svalbard) during the Decade 2007–2017

Barbara Barzycka[1,*], Mariusz Grabiec[1], Małgorzata Błaszczyk[1], Dariusz Ignatiuk[2,1], Michał Laska[1], Jon Ove Hagen[3] and Jacek Jania[1]

[1] University of Silesia in Katowice, Faculty of Natural Sciences, Institute of Earth Sciences, Poland;

[2] Svalbard Integrated Arctic Earth Observing System - Knowledge Centre (SIOS-KC), Norway;

[3] Department of Geosciences, University of Oslo, Norway.

[*] Correspondence: bbarzycka@us.edu.pl

ABSTRACT

Changes in glacier facies (glacier zones), such as firn or superimposed ice, are good indicators of glacier response to climate change. They are especially important for fast-warming Svalbard, where only a few glaciers are under glaciological mass balance monitoring. This paper presents a first study of changes of glacier facies extent for three tidewater glaciers located in southern Spitsbergen, Svalbard.

The study is based on both satellite remote sensing and terrestrial data analysis and covers two time spans: 2007–2017 for Hansbreen and 2012–2017 for Storbreen and Hornbreen. Glacier facies extents are distinguished by means of classification of Synthetic Aperture Radar (SAR) data from both decommissioned (ENVISAT ASAR) and modern satellite missions (RADARSAT-2, Sentinel-1, ALOS-2 PALSAR). The results of the SAR classification are compared to the information on glacier zones retrieved from shallow cores and visual interpretation of 800 MHz Ground Penetrating Radar (GPR) data. In addition, a novel application of the Internal Reflection Power (IRP) coefficient is discussed. Changes in glacier facies areas over time are analysed, as well as their correlation to Hansbreen's mass balance.

The main finding of the study is that the accumulation area (i.e. firn and superimposed ice) of Hansbreen, Storbreen and Hornbreen significantly decreased over the study period. For example, due to continuous negative mass balance between 2010 and 2017, the contribution of firn area to Hansbreen's total area decreased ca. 14% (cumulative firn area loss during that time: ~44%). In addition an east–west gradient of firn area loss was observed as a result of differences in local climate conditions. Therefore, for the common time span (i.e. 2012–2017) Hansbreen recorded a ca. 12% loss of firn contribution to glacier area whereas Hornbreen recorded ca. 9%. Finally, application of the IRP coefficient as an objective method of glacier zones discrimination by GPR data gave very good results, so the method is recommended for future analysis of glacier zones.

Keywords: glacier zones, glacier facies, firn, superimposed ice, mass balance, Internal Reflection Power (IRP), Ground Penetrating Radar (GPR), Synthetic Aperture Radar (SAR), Hornsund, Svalbard.

1 INTRODUCTION

Svalbard archipelago, located in the Arctic, is one of the fastest-warming places on Earth (Serreze and Francis 2006; Nordli et al. 2014). Svalbard is warming ca. 0.81°C per decade (Vikhamar-Schuler et al. 2019), and one of the highest average air temperatures on the archipelago occurs in the southwest part of Spitsbergen, the main island of Svalbard (Vikhamar-Schuler et al. 2019). Glaciers located in this area are significantly retreating (e.g. Błaszczyk et al. 2013; Nuth et al. 2013; Szafraniec 2018), thinning (e.g. Moholdt et al. 2010; Nuth et al. 2010; Ignatiuk et al. 2014; Błaszczyk et al. 2019a) and losing mass (e.g. Hagen et al. 2003; Østby et al. 2017; van Pelt et al. 2019; WGMS 2019). These ongoing changes, forced by distinct warming, may be especially important for understanding the future of larger land ice masses. Therefore, monitoring of changes in Svalbard's glaciers and their components may be important for studies of ice sheets and ice caps as small-scale analogues.

One component of the glacier system which is sensitive to climate change is the extent of glacier facies. Glacier facies (Benson 1961; Müller 1962) – also referred as glacier zones – differ in their structure, density, percolation properties, heat conductivity and the albedo of the surficial glacier layer. Thus, information on their extents could support understanding of numerous glacier properties and processes including: mass balance (e.g. Müller 1962; Dyurgerov et al. 2009), water drainage (e.g. Jansson et al. 2003; Decaux et al. 2019), surface energy balance (e.g. Braun and Hock 2004; Hoffman et al. 2008) or microbiology of glacier habitats (e.g. Hodson et al. 2008; Boetius et al. 2015).

Under recent glacier mass loss, zones such as firn or superimposed ice are of special importance. Together with snow zone (if present), they build the accumulation zone of a glacier, i.e. an area where mass gain exceeds loss. In addition, firn, due to its porous structure, has higher retention capacity than e.g. ice. Therefore, rain- or meltwater may be stored in firn aquifer in both liquid and (after freezing) solid form (Hagen et al. 2003; Jansson et al. 2003). Superimposed ice, on the other hand, forms on the surface of glacier ice as a layer of refrozen water coming from meltwater or rain events (Baird, 1952), also preventing its immediate runoff from the glacier system (Woodward et al. 1997). Due to the continuous negative mass balance of glaciers, changes in glacier zone contribution can be expected.

Although field data undoubtedly provide invaluable information on a glacier’s state, satellite remote sensing methods are an approach to enrich them by providing information from vast and inaccessible areas. Although glacier zones have been detected by analysis of multispectral images during the ablation season (e.g. Hall et al. 1987; Pope and Rees, 2014; Laska et al. 2017a; Sobota and Wójcik 2020), for detection of their annual changes and possible support of mass balance studies Synthetic Aperture Radar (SAR) data are advantageous. SAR is an active system operating in the microwave range of the electromagnetic spectrum. As a result, the SAR signal is independent of sunlight and penetrates through the dry snow cover, reaching the glacier surface and subsurface (Hall, 1996; Rignot et al. 2001; Tebaldini et al. 2016). Therefore, glacier monitoring can also be run during polar night, when under accumulated snow cover a previous summer surface from the end of the ablation season is preserved.

Studies of glacier facies extents, derived from SAR and compared to terrestrial data, cover only a few locations in Svalbard. These include Kongsvegen and neighbouring glaciers, located in western Spitsbergen (e.g. Engeset et al. 2002; König et al. 2002, 2004; Brandt et al. 2008; Langley et al. 2008; Akbari et al. 2014), and two ice caps in north-eastern Svalbard: Austfonna (Dunse et al. 2009) and Vestfonna (Błaszczyk, 2012; Barzycka et al. 2019). Grabiec (2017) distinguished facies of Hansbreen in southern Svalbard in 2008. Another approach was presented by Winsvold et al. (2018), where extents of glacier facies along the main axis of Kongsvegen and on neighbouring Holtedahlfonna were delivered by SAR. Few studies of Svalbard's glacier facies cover a long time span and most of them are related to Kongsvegen and its neighbourhood. For example, Engeset et al. (2002) studied glacier zones of Kongsvegen between 1991 and 1997, König et al. (2004) analysed changes in firn area of this and neighbouring glaciers between 1992 and 2003, whereas Winsvold et al. (2018) analysed changes of zones along main axes of Kongsvegen and Holtedahlfonna between 2009 and 2016. Dunse et al. (2009) analysed glacier facies extent along several transects on Austfonna between 2004 and 2007.

The glacier zones distinguished by SAR analysis are often compared to results of *in situ* measurements. One of the most common sources of additional information in such research is shallow drilling cores (e.g. Engeset et al. 2002; König et al. 2002) and Ground Penetrating Radar surveys (GPR; e.g. Engeset et al. 2002; Langley et al. 2007, 2008; Brandt et al. 2008; Barzycka et al. 2019). These methods, however, have some limitations. Shallow cores deliver information from one particular point, sometimes influenced by local topography. GPR profiles are often visually interpreted, making them dependent on the experience and subjectivity of the operator. To our knowledge, there are few exceptions to this. Langley et al.

(2007, 2008) compared backscatter signatures of SAR and GPR for analysis of reflection sources of the two systems within GPR visually interpreted glacier facies, whereas Grabiec (2017) and Barzycka et al. (2019) classified a GPR Internal Reflection Energy (IRE; Jania et al. 2005) coefficient as an alternative to the GPR visual interpretation of glacier zones.

The main goal of the study is to identify long-term changes in the glacier facies area of three glaciers in the Hornsund basin: Hansbreen, Storbreen and Hornbreen. The relationship between Hansbreen's zones extent and glacier mass balance has to be determined and discussed. This is a first study of changes in glacier facies over time for southern Spitsbergen and a first attempt to distinguish glacier zones on Storbreen and Hornbreen. In addition, as this research covers a decade of direct measurements (cores, GPR) and SAR acquisitions, it is also one of few long time series of distinguishing glacier facies for the Svalbard archipelago. For *in situ* measurements, a novel application of the Internal Reflection Power (IRP) coefficient of GPR data is tested and discussed in detail as an alternative to popular yet demanding visual interpretation of glacier zones on GPR profiles. The SAR data analysed in this study are of different capacity with regard to e.g. polarimetry mode, resolution or pixel spacing. Therefore, the advantages and limitations of distinguishing glacier zones by different-quality SAR images and the applied classification methods are further discussed.

2 STUDY AREA

Hansbreen, Storbreen and Hornbreen (Figure 1) are polythermal tidewater glaciers terminating into Hornsund, the southernmost fiord of Spitsbergen island. The glaciers are valley-type, with south (Hansbreen, Storbreen) or south-west (Hornbreen) orientation and low slope inclination along centrelines (1.3° for Storbreen and Hornbreen and 1.7° for Hansbreen) (Błaszczyk et al. 2013).

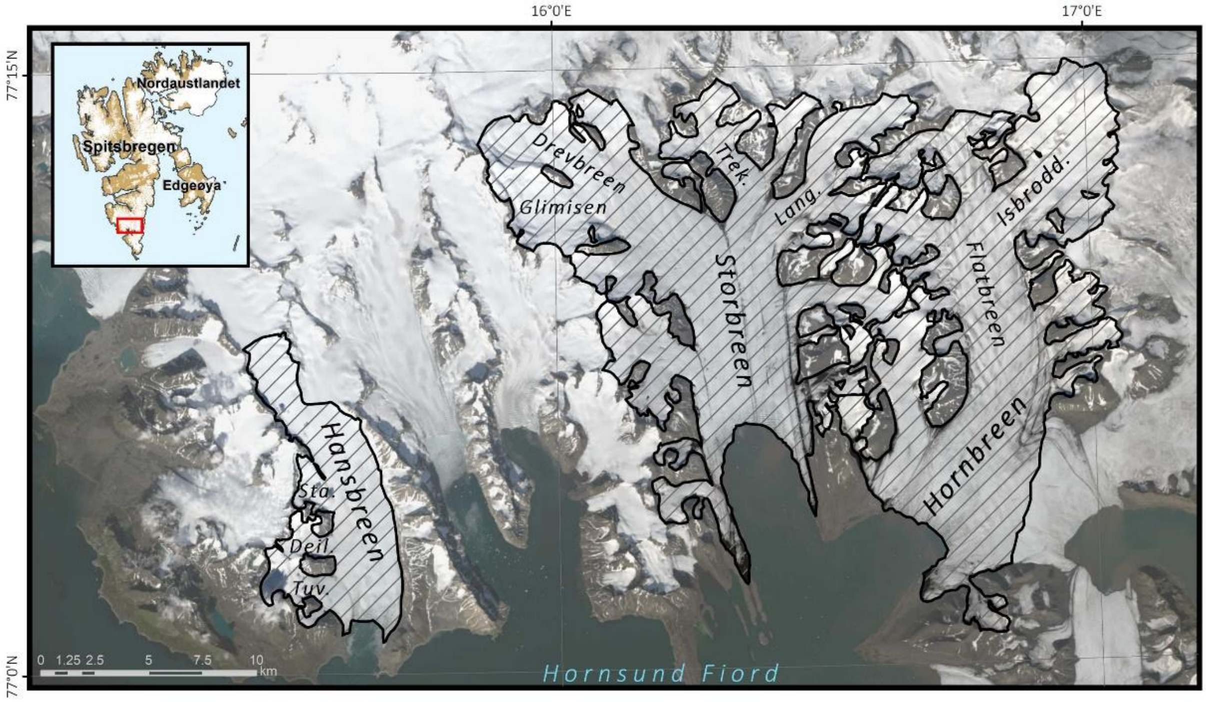

Figure 1 Location of analysed glaciers with their main tributaries (marked by black outlines) Abbreviations: Tuv. – Tuvbreen, Deil. – Deileggbreen, Sta. – Staszelisen, Trek. – Trekløverbreen, Lang. – Langleikbreen, Isbrodd. – Isbroddbreen. Landsat 8 courtesy of the U.S. Geological Survey, overview map provided by the Norwegian Polar Institute (npolar.no).

Hansbreen is one of the most widely studied land ice masses in Svalbard, being included in the World Glacier Monitoring Service (WGMS) network since 1989. The west side of Hansbreen is fed by four tributary glaciers: Fuglebreen, Tuvbreen, Deileggbreen and Staszelisen (Grabiec et al. 2012). In 2010 the glacier covered an area of 53.9 km^2 (Błaszczyk et al. 2013) with a mean ice thickness of 171 m and volume ~9.6 km^3 (for 2004: Grabiec et al. 2012). The average Equilibrium-Line Altitude (ELA) of Hansbreen was detected at 342 m a.s.l. in 2014 (Laska et al. 2017a). The snow accumulation at the main trunk of the glacier is asymmetrical, favouring the western over the eastern side (e.g. Grabiec et al. 2011; Grabiec 2017; Laska et al. 2017b). Hansbreen’s front average velocity in 2012 was estimated at 177 m a^{-1} (Błaszczyk et al. 2019b).

Storbreen, located in the central part of Hornsund fiord, is a glacier of 196.5 km^2 surface area (in 2010: Błaszczyk et al. 2013). Over 10 tributary glaciers feed Storbreen, among them large

Glimisen, Drevbreen, Trekløverbreen and Langleikbreen in the northern part of the glacier. The ELA in 2014 was located at 383 m a.s.l. (Laska et al. 2017a). Storbreen's average frontal velocity in 2014 was estimated at 132 m a^{-1} (Błaszczyk et al. 2019b).

The easternmost of the analysed glaciers is Hornbreen, with the main contribution coming from Flatbreen and its tributary glaciers (Isbroddbreen as the main accumulation area). The size of the glacier in 2010 was assessed at 176.2 km^2 (Błaszczyk et al. 2013) whereas the ELA in 2014 was 398 m a.s.l. (Laska et al. 2017a). Hornbreen has the highest average frontal velocity of the analysed glaciers: 287 m a^{-1} (for 2014: Błaszczyk 2019b). A recent study by Grabiec et al. (2018) shows that the glacier system of Hornbreen and adjacent Hambergbreen is located over a subglacial depression, which, if the retreat of the glaciers continues, will create a new strait in the Svalbard archipelago.

3 DATA

3.1 SYNTHETIC APERTURE RADAR

During the decade analysed here, changes in the SAR temporal resolution were noted, from poor coverage of the Arctic in the past to more complete coverage recently. SAR images were provided by both decommissioned (ENVISAT ASAR) and modern satellite missions (RADARSAT-2, Sentinel-1, ALOS-2 PALSAR; Table 1). For each analysed year, up to five available SAR images acquired during an accumulation season and close to the date of *in situ* measurements were chosen for the analysis. This choice of dates (winter and spring) was made in order to prevent the water content in snowpack present during the melting season, or rain, greatly affecting backscattering of the SAR signal (Rott and Mätzler, 1987; Winsvold et al. 2018). In addition, SAR images characterized by high polarization mode, high resolution and small spacing were preferred as they provide more complex information than e.g. a single-polarization and large pixel size SAR image. All data were acquired from ascending orbits. The range of incidence angles was similar in each set of SAR images for a given year. When possible, Single Look Complex (SLC) data were chosen for study purposes. If these were inaccessible, detected, multi-looked, ground range SAR products were analysed: ENVISAT ASAR Wide Swath Mode Medium Resolution (WSM), RADARSAT-2 SAR Georeferenced Fine (SGF) and Sentinel-1 Ground Range, Multi-Look, Detected (GRD) data (Harris 1998; Kult 2012; Maxar Technologies Ltd. 2018; Vincent et al. 2019).

Table 1. SAR data processed in this study. Acronyms: Prev. S. S. – year of previous summer surface; abs. – absolute; incid. – incidence; WSM – Wide Swath Mode Medium Resolution; SGF – SAR Georeferenced Fine; GRD – Ground Range, Multi-look, Detected; SLC – Single Look Complex. Source of information marked as: [1]metadata of the SAR data files, [2]Kult (2012), [3]Bourbiguot et al. (2016), [4]Japan Aerospace Exploration Agency (2016) and [5]Maxar Technologies Ltd. (2018). Near and far incidence angles of IW mode data were provided only for processed sub-swaths, not whole SAR scenes.

PREV. S. S.	MISSION	BAND	POLARIZATION[1]	RANGE x AZIMUTH SPACING [m]	RESOLUTION [m]	MODE[1]	TYPE[1]	DATE[1]	ABS. ORBIT[1]	NEAR INCID. ANGLE [°][1]	FAR INCID. ANGLE [°][1]
2007	ENVISAT ASAR	C	HH	75.0 x 75.0[2]	150.0 x 150.0[2]	ASAR Wide Swath	WSM	3 APR '08	31860	16.25	42.93
								3 APR '08	31860	16.25	42.93
								3 APR '08	31860	16.26	42.93
2010	RADARSAT-2	C	HH HV	50.0 x 50.0[5]	163.0-73.0 x 78.0-106.0[5]	ScanSAR Wide	SGF	25 FEB '11	16708	19.47	49.43
2012	RADARSAT-2	C	HH HV	25.0 x 25.0[5]	81.0-44.0 x 40.0-50.0[5]	ScanSAR Narrow	SGF	11 APR '13	27798	19.65	39.55
								21 APR '13	27941	19.66	39.55
2013	RADARSAT-2	C	HH HV	25.0 x 25.0[5]	55.0-38.0 x 58.0-70.0[5]	ScanSAR Narrow	SGF	22 MAR '14	32729	30.77	46.60
								5 APR '14	32929	30.76	46.59
2014	Sentinel-1	C	HH HV	40.0 x 40.0[3]	93.0 x 87.0[3]	Extra-Wide (EW)	GRD	30 MAR '15	5257	19.14	46.46
								31 MAR '15	5272	19.20	46.49
								1 APR '15	5292	19.20	46.45
								2 APR '15	5301	19.12	46.45
								2 APR '15	5307	19.31	46.46
2015	Sentinel-1	C	HH	2.3 x 14.1[3]	2.7-3.5 x 22.0[3]	Interfero-metric Wide (IW)	SLC	22 FEB '16	10061	30.22	48.07
								5 MAR '16	10236	30.22	48.07
								29 MAR '16	10586	30.22	48.07
								10 APR '16	10761	30.23	48.08
								22 APR '16	10936	30.23	48.08
2016	ALOS-2 PALSAR	L	HH HV VV VH	2.9x3.2[4]	5.1 x 4.3[4]	Stripmap High-sensitive	SLC	10 APR '17	15566	32.37	35.35

2017	Sentinel-1	C	HH HV	2.3 x 14.1[3]	Interfero-metric Wide (IW)	SLC	1 MAR '18	9840	30.27	50.07
							13 MAR '18	10015	30.22	50.07
							25 MAR '18	10190	30.22	50.07
				2.7-3.5 x 22.0[3]			6 APR '18	10365	30.22	50.07
							18 APR '18	10540	30.23	50.07

Available precise orbit files were used for refining orbit vectors of SAR data (Doornbos et al. 2002; Peter et al. 2017). All analysed images were radiometrically calibrated (Rosich and Meadows 2004; Shimada et al. 2009; Miranda and Meadows 2015; MacDonald, Dettwiler and Associates Ltd. 2016). Due to glacier thinning (and consequent changes of glacier elevations), a SPOT Digital Elevation Model (DEM) from 2008 (Błaszczyk et al. 2019a) was used for terrain correction (Small and Shubert 2008; Caves and Williams 2015) of 2008 and 2011 data. In the case of SAR images acquired after 2011, the ArcticDEM (Porter et al. 2018) was implemented to the terrain correction algorithm (Shimada et al. 2009; Caves and Williams 2015; Small and Shubert 2019). In addition, prior to the terrain correction, from Sentinel-1 Interferometric Wide (IW) SLC products only sub-swaths covering the area of research were chosen for further processing, debursted, merged and multi-looked to ground range square pixel (Small and Shubert 2019). To reduce speckle noise of the SAR images, sets of more than one SAR datum in a year were averaged into one image (Langley et al. 2008; Barzycka et al. 2019), and a Refined Lee speckle filter (Lee and Pottier, 2009) was applied to all SAR data except the Hansbreen 2008 SAR dataset. Due to the high noise of averaged SAR images of the latter, an Improved Lee Sigma speckle filter was used (Lee et al. 2009).

For H–α Wishart classification purposes, quad-polarimetry ALOS-2 PALSAR complex data were multi-looked to ground range square pixel. In addition – necessary for further classification – a coherency matrix was generated (Cloude and Pottier, 1996) and terrain-corrected by the ArcticDEM.

3.2 GROUND PENETRATING RADAR

All ground-based radio-echo soundings data analysed in this study were collected by GPR equipped with an 800 MHz frequency shielded antenna. The GPR set was pulled behind a snowmobile on a sledge at a speed of ~20 km h^{-1}. Simultaneously with the GPR surveys, GPS positions were collected by a GPS rover fixed to the GPR set at a constant time interval varying between GPR datasets from 0.2 to 1.0 s. Average distances between GPR traces attributed to GPS positions varied between GPR datasets but oscillated around 1 m per GPR dataset, with the exception of the Hansbreen 2008 dataset (2.8 m; Table 2). The inequality in average distances was caused mainly by differences in settings of the GPR/GPS data collection intervals between GPR datasets.

Table 2 Details of 800 MHz Ground Penetrating Radar surveys used in the study. Acronym: Prev. S. S. – year of previous summer surface.

PREV. S. S.	GLACIER	DATE	TOTAL LENGTH [km]	SAMPLING FREQUENCY [MHz]	STACKS	AVERAGE DISTANCE BETWEEN TRACES [m]
2008	HANSBREEN	26 APR ‘08	62.3	5116.6	8	2.5
2011	HANSBREEN	14, 17 APR ‘11	110.2	12791.6	8	1.4
2013	HANSBREEN	16, 17 APR ‘13	107.9	12791.6	8	0.9
	STORBREEN	20 APR ‘13	12.3	12791.6	8	0.9
	HORNBREEN	20 APR ‘13	11.8	12791.6	8	1.0
2014	HANSBREEN	3, 12 APR ‘14	105.1	12791.6	8	1.0
	STORBREEN	13 APR ‘14	15.7	12791.6	8	1.1
	HORNBREEN	5 APR ‘14	12.2	12791.6	8	0.8
2015	HANSBREEN	2 APR ‘15	98.4	5149.2	4	1.1
2016	HANSBREEN	18 APR ‘16	94.0	8183.6	4	1.3
2017	HANSBREEN	22 APR ‘17	100.2	12791.6	8	1.7
2018	HANSBREEN	18 APR ‘18	104.8	16410.2	4	1.2
	STORBREEN	26 APR ‘18	25.0	12763.5	4	1.2
	HORNBREEN	26 APR ‘18	22.8	16410.2	2	1.1

All GPR measurements were performed under dry snow conditions to ensure optimal propagation of the GPR signal within analysed structures (Grabiec 2017). Maximal depth penetration of both snow cover and underlying features by the GPR signal was limited by the time window (two-way travel time in range 67.03–148.33 ns; depending on the survey season and glacier). GPR tracks cover both accumulation and ablation areas of Hansbreen including its tributary glaciers, and have been repeated since 2011, reaching an average total length of GPR profiles in a GPR dataset of 103 km (Table 2). In 2013, GPR cross-sections via facies of Storbreen and Hornbreen were obtained by respectively 12.3 and 11.8 km of GPR profiles along glaciers' main axes, and they were repeated during subsequent field campaigns. In 2018 the coverage of Storbreen's axis was limited to 3.31 km due to technical problems of GPR setting caused by very low-temperature conditions. However, prior to this, 9.45 km of additional GPR profiles were collected on Storbreen's main trunk.

The GPR files were collected at different measurement settings, varying in time-window, sampling frequency, stacking and trace intervals. Thus, they were properly processed prior to visual interpretation and IRP calculation. The first data-processing step included removing corrupted parts of the GPR profiles (e.g. due to low voltage of the batteries), time-window unification and basic files preparation for further filtering. After time-zero setting, the radar profiles were cut in time domain, skipping all content in the interval between 1.2 ns before and 76 ns after first break. This procedure was applied to all profiles except those acquired in 2018 at Hornbreen, as the original time window was narrower (67.03 ns). The DC was then calculated based on a 61–76 ns time range. After the initial file preparation described above, the main processing included bandpass filtering, signal amplification and subtraction in distance domain. The bandpass filtering passing signal was in the range 400–1200 MHz. The signal amplitude was then corrected against signal strength loss due to its geometrical spreading. Finally, a 51-trace moving average amplitude was subtracted from individual traces in order to remove horizontal artefacts (e.g. due to direct wave). The latter procedure is not valid for the first and terminal 25 traces, which are excluded from further interpretation and processing. The GPR traces were assigned to the GPS positions gathered by the external GPS receiver. Due to differences in temporal sampling interval between the GPS receiver and GPR set, the interval was upscaled to 1 s in order to combine both datasets.

3.3 SHALLOW GLACIER CORES

Six shallow cores on Hansbreen's surface along its centreline were retrieved on 11 April 2016 and six cores in the vicinity of the ELA on 18 April 2017. On 22 and 26 April 2018, eight, five and four shallow cores were drilled along the main axes of Hansbreen, Storbreen and Hornbreen respectively. The cores consisted of seasonal snow cover and underlying structures of glacier ice, superimposed ice or firn which were visually interpreted taking into account the size of firn granules, ice crystals and their texture and pattern. Attention was paid to snow depth and the presence of ice layers in it. The diameter of the used corer was 9 cm. The length of the cores varied depending on the snow cover thickness, but was made sufficiently long for the interpretation of the structures buried under snow, representing the previous summer surface.

4 METHODS

4.1 GPR VISUAL INTERPRETATION (GPR VI)

The GPR profiles have been analysed to separate the glacier facies. The upper layer of every profile referred to the snow is excluded from the interpretation. Recognition of the snow cover does not pose any major difficulties as it forms a superficial continuous layer of higher reflection properties and horizontal layering. The snow-ice/firn interface was determined manually in every GPR profile and then applied as the upper limit of the IRP calculation. The procedure of snow cover determination from the GPR profiles as well as its spatial variability over analysed glaciers is presented by Grabiec et al. (2011), Laska et al. (2017b) and Uszczyk et al. (2019).

The sub-snow glacier structure has been divided into three classes: ICE, SI and FIRN representing ice, superimposed ice and firn zone respectively. In further text the capital letters (FIRN, SI, ICE) refer to results of direct analysis of *in situ* data (i.e. GPR VI and shallow glacier cores), whereas lower case (firn, superimposed ice, ice) refers to glacier zones in general terms.

The ICE includes a wide range of structures generally characterized by a low amount of scattering or reflecting objects within the glacier body. A pure ice block is free of scattering elements; however, due to discontinuities in the glacier surface (e.g. crevasses, moulins), englacial conduits and pockets, debris bands incorporated into the ice, ice foliation and other features, the ICE may contain some sections of increased reflectivity.

The SI forms a rather shallow (up to a few metres) layered structure of mediate reflection properties between ICE and FIRN. Superimposed ice contains more air holes and airbladders as an effect of rapid freezing at atmospheric pressure. The SI location is mostly transitional between ICE and FIRN. Some sections are noted in a depression below the firn area as residues of larger early summer SI covers mostly melted out till the end of the ablation season. The SI/ICE interface is well defined, but reflectance is lower than at the snow/ICE boundary surface.

The FIRN is characterized by a high-reflection, mostly layered pattern (but chaotic structure can be noted as well). Starting from the firn line, the firn gradually thickens up, becoming thicker than the GPR profile's time window after a few hundred metres. In profiles containing continuous firn some shallower sections may be recognized, but still classified as FIRN if any portion of firn lies below the snow cover.

As GPR data analysed in this study provide information on glacier facies extents at the end-of-previous-summer surface, the results of the GPR VI refer to the year of the last ablation season, not the ongoing accumulation season.

4.2 INTERNAL REFLECTION POWER

Internal Reflection Power (IRP), first introduced by Gades et al. (2000), is a mean value of reflected energy for a sample within a defined time window of a GPR trace. IRP can be described by the equation below (Gades et al. 2000):

$$IRP \equiv 0.5 * \frac{\sum_{i=t_1}^{t_2} A_i^2}{(n(t_2) - n(t_1) + 1)}$$

where: A_i – amplitude of an i sample, t_1 – time of the first sample within the defined time window, t_2 – time of the last sample within the defined time window.

IRP has been widely applied to studies of glacier bedrock, ice properties and water presence in glacier systems (e.g. Copland and Sharp 2001; Catania et al. 2003; Jania et al. 2005; Navarro et al. 2005; Matsuoka et al. 2007; Pattyn et al. 2009; Gacitúa et al. 2015) but not in distinguishing glacier facies. On the other hand, a modification of IRP – the Internal Reflection Energy (IRE) (Jania et al. 2005) – was successfully implemented in research of glacier facies by its classification (Grabiec 2017; Barzycka et al. 2019). IRE – one-half of the sum of squared amplitudes within a defined time window – is a value strongly dependent on a number of samples in the time window. Therefore, it should not be applied in studies which include comparison of the IRE calculated based on GPR datasets collected with different sampling frequency or stacking (Table 2). IRP, an arithmetic mean, is less sensitive to those differences than IRE. As this study covers a decade of GPR measurements in Hornsund fiord basin, performed under various sampling frequencies and stacking (Table 2), IRP was applied as an alternative to GPR visual interpretation.

In addition, by applying the IRP equation to the first 2 ns of each GPR trace, a noise power (NP) (Jania et al. 2005; Grabiec 2017; Barzycka et al. 2019) was calculated as well as its median for every GPR profile (i.e. traces recorded during a continuous measurement, saved in one file). The GPR background noise for a profile, represented by the median NP, varied significantly in a GPR dataset, influencing IRP. This was resolved by normalization of GPR amplitudes by a coefficient calculated as the median of absolute values of amplitudes in the first 2 ns of a GPR dataset divided by the median of absolute values of amplitudes in the first 2 ns for a GPR profile (i.e. GPR file).

For IRP calculation a time window of 25.8 ns was applied. This time range was set to ensure that all features will be taken into account in the IRP calculation. As suggested in Barzycka et al. (2019), the time window was not fixed but moving. Therefore, the beginning of the IRP calculation depended on the thickness of snow in a trace. This was especially important for analysed glaciers as the snow cover depth varies not only within each glacier basin separately (Grabiec et al. 2006, 2011; Grabiec 2017, Laska et al. 2017b) but also between them (Laska et al. 2017b). As a snow-cover/glacier boundary (i.e. previous summer surface) was manually detected and is characterized by high amplitude values which may influence IRP, an additional 1 ns margin (an equivalent of ~1 cm of ice penetration) from the glacier/snow-cover boundary was applied. Therefore, the beginning of the IRP calculation was set at 1 ns below the snow cover for every trace. Finally, IRP values were moving-averaged by a window containing GPR samples on a horizontal ca. 50 m distance.

The results of the IRP calculation are presented in the form of boxplots and scatter plots for GPR profiles along the glaciers' axes (Barzycka et al. 2019). In addition, IRP was classified by the natural breaks (Jenks) method (Jenks and Caspall 1971; de Smith et al. 2007) and the results are presented in the form of maps. The initial number of classes was set at three (i.e. IRP ICE, IRP SI, IRP FIRN); if classification quality was poor, the number of classes was lowered to two, as a representation of IRP ICE and IRP FIRN. The accuracy of the IRP natural breaks classification method was determined by calculating the following measures: user's accuracy (UA), producer's accuracy (PA), F-score (F) and Kappa (K; Lillesand et al. 2008). User's accuracy is the probability that a classified sample truly represents this class, whereas producer's accuracy is the probability that samples from a given category (i.e. glacier zone) were correctly classified. The F-score is a harmonic mean of user's and producer's accuracies and describes the overall accuracy of a category's classification. Finally, as a measure of a dataset's classification accuracy, Kappa was calculated. Kappa is a statistic describing how a performed classification differs from a random classification (Lillesand et al. 2008).

Similarly to the results of the GPR VI, the results of IRP analysis refer to the year of the last ablation season, not the year of data collection.

4.3 SAR CLASSIFICATION

The highly diverse SAR data of this study required a choice of such a classification method, which could be applied to a GRD (i.e. level reached also by pre-processed SLC) SAR image of either single- or dual-polarimetry mode. For this purpose, a combination of Iterative Self-Organizing Data Analysis Technique (ISODATA) and Maximum Likelihood Classification (MLC; Ball and Hall 1965; Lillesand et al. 2008) was applied. ISODATA is a variant of the unsupervised K-means clustering method where, based on a cluster's statistical similarity, an initial number of classes can be reduced after each algorithm's iteration. This allows determination of more natural and objective spectral groupings of data than K-means. MLC, on the other hand, is a supervised classification method which – based on means and covariance matrixes provided by unsupervised ISODATA clustering – assigns a given data point to a class with the highest probability of membership for that point. The combination of ISODATA and MLC has been applied in various studies with good results (e.g. Sulebak et al. 1997; Hall et al. 1998; Townsend et al. 2009; Jones et al. 2014; Ganju et al. 2017).

The combination of ISODATA and MLC (ISODATA+MLC) classification of single- and dual-polarization SAR images was limited to the areas of the analysed glaciers derived from Błaszczyk et al. (2013). As the fronts of Hansbreen, Storbreen and Hornbreen have retreated over time (Błaszczyk et al. 2019b), this part of the glaciers' outlines was continuously updated based on SAR imagery. Prior to the classification of dual-polarization images, the HV band was normalized by linear transformation to a larger range of HH data (Jones et al. 2014; Environmental Systems Research Institute 2017). A random number of a maximum 20 initial clusters and a minimum cluster size of 2.5% of a glacier's area were set for the ISODATA clustering. This choice of settings was made in order to ensure that the results of the ISODATA clustering would represent the natural grouping on the data, uninfluenced by the subjectivity of operator's choices. Information on clusters' characteristics derived from ISODATA clustering was implemented to MLC as training sites. The results of ISODATA+MLC were aggregated (Lillesand et al. 2008) into three classes: SAR ICE, SAR SI and SAR FIRN. The aggregation process was dependent on dendrograms (i.e. a diagram of distances between pairs and groups of clusters), general knowledge of glaciers (e.g. small probability of firn presence at low elevation and in the vicinity of Svalbard's tidewater glaciers' fronts), multispectral imageries from ablation seasons (Landsat 7, 8; Sentinel-2; aerial photos and Very High Resolution Images from Błaszczyk et al. 2019b), DEMs and GPR VI. Finally, a careful manual reclassification of some features was required. This was mainly due to high values of the SAR backscatter coefficient in crevassed or debris areas (SAR FIRN/SI to SAR ICE reclassification) or low values in shadowed accumulation areas (SAR ICE to SAR FIRN reclassification). The manual correction was supported by the sources of information as in the aggregation process.

An exception to SAR data classified by the ISODATA+MLC method was an ALOS-2 PALSAR quad-polarimetry image acquired in 2017. In order to fully exploit information delivered by the SLC quad-polarimetry image, an unsupervised H–α Wishart classification (Cloude and Pottier 1997; Lee et al. 1999) was applied. This algorithm is designed for Single Look Complex data and takes into account not only amplitude but also phase of the SAR backscattered signal (information lost in GRD data) registered for all four polarizations (HH, HV, VH, VV). Therefore, the input information and classification algorithm is more comprehensive than in the case of data classified by ISODATA+MLC. As a result, based on entropy (*H*) and mean alpha (*α*) angle (representation of SAR scattering mechanism), up to eight classes of different scattering behaviours can be identified. As glacier zones are characterized by different scattering properties, the H–α Wishart classification has already been successfully applied to glacier facies extent detection by Błaszczyk (2012) followed by Barzycka et al. (2019).

The H–α Wishart classification was performed in the open-source PolSARPro 5.1 software (Pottier and Ferro-Famil, 2012). Prior to the classification, necessary H–α decomposition of the pre-processed ALOS-2 PALSAR data was carried out (Cloude and Pottier, 1996). Generated entropy and mean alpha angle parameters were used for the H–α Wishart classification. Similarly to ISODATA+MLC, the results of H–α Wishart classification were aggregated to classes representing glacier facies and carefully manually corrected in crevassed and shadowed areas.

Final results of SAR classification are presented in the form of maps and compared to the results of the GPR visual interpretation and IRP classification. SAR classification's accuracy is discussed based on calculated user's and producer's accuracies, F-score and Kappa with GPR VI as reference data. All results are presented in reference to the year of previous summer surface, not of data collection.

4.4 Analysis of changes in areas of glacier facies

Based on the results of SAR classification, areas of glacier zones in each SAR dataset have been retrieved. In addition, as analysed glaciers are tidewater, their fronts' positions (and thus also glacier areas) are subject to dynamic changes (Błaszczyk et al. 2013). Because of that, a percentage contribution of each zone to a glacier's total area has been calculated (König et al. 2004). This measure is referred to further in the text as "contribution".

The changes of glacier zones areas were analysed for two periods of time. The first time span is set from 2007 to 2017 summer surface and covers a decade of changes on Hansbreen. The second time span is from 2012 and 2017 summer surface, i.e. the time span common for Storbreen, Hornbreen and Hansbreen as well. In addition, a percentage gain or loss of area of each glacier zone was calculated as a ratio between the area of a zone at the end and at the beginning of an analysed time span.

Finally, encouraged by results of high correlation between Kongsvegen's mass balance and either its firn area (König et al. 2004) or ELA (Engeset et al. 2002), the correlation between Hansbreen's net mass balance (WGMS, 2019) and its accumulation area (i.e. SAR SI and SAR FIRN) has been analysed.

5 RESULTS

5.1 GPR VISUAL INTERPRETATION

Examples of GPR visual interpretation of Hansbreen's main longitudinal GPR profile have been studied and are presented in Figure 2. High reflectivity in the FIRN class can be noted, as well as general low reflectivity in ICE. In addition, a GPR profile obtained for the 2010 previous summer surface contains the only example of SI (layered structure of medium reflectivity) – later this class was not present on GPR profiles along Hansbreen's main axis.

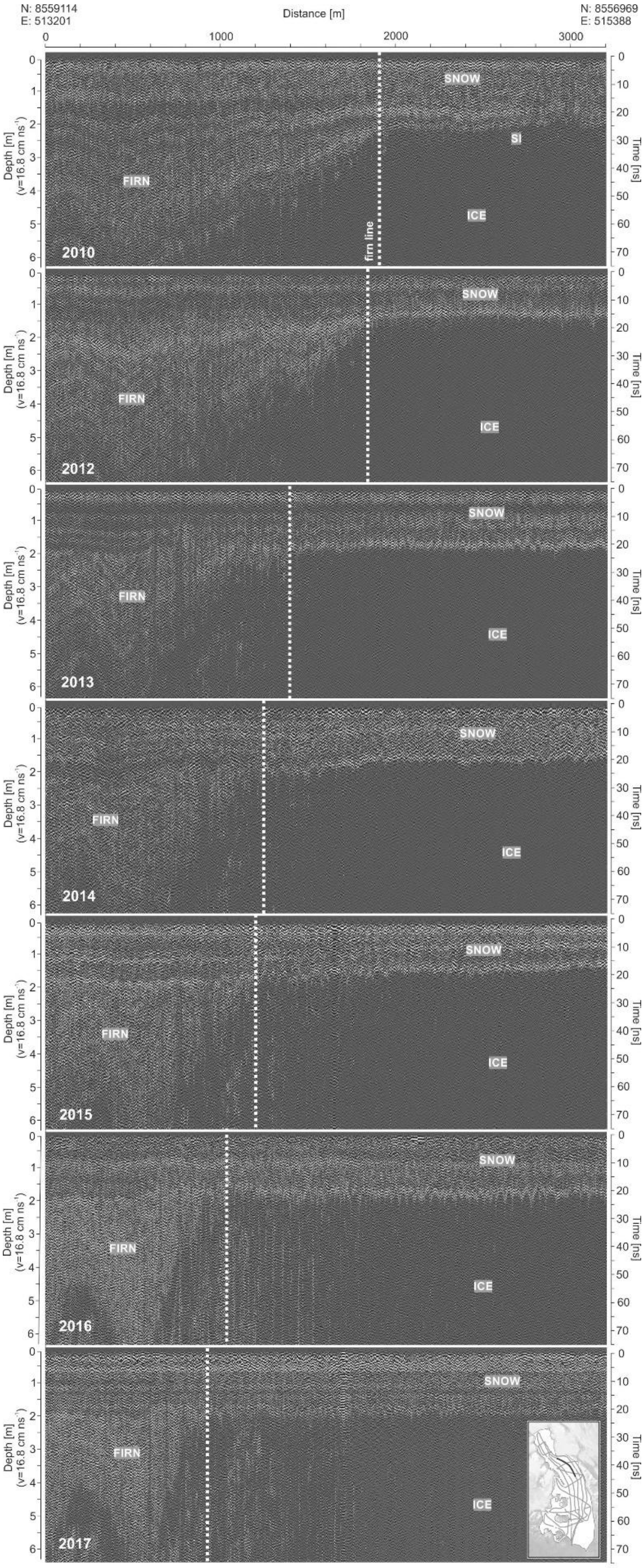
N: 8559114
E: 513201
Distance [m]
N: 8556969
E: 515388
0
1000
2000
3000
Depth [m]
(v=16.8 cm ns⁻¹)
Time [ns]
SNOW
SI
FIRN
ICE
firn line
2010
2012
2013
2014
2015
2016
2017

Figure 2 Results of GPR visual interpretation superimposed on GPR profiles obtained along a main axis of Hansbreen between 2011 and 2018. Years refer to the previous summer surface, not the year of GPR measurements. Spatial location of the GPR profiles is presented on an overview map.

Between 2010 and 2017, the firn line along Hansbreen’s axis retreated over 900 m, with its maximum between 2012 and 2013 (ca. 300 m). In addition, a change in FIRN structure can be noted – from a distinctly layered pattern between 2010 and 2013 to a rather chaotic structure in 2016 and 2017. Finally, since 2015, ICE sections below the firn line are characterized by a relatively high amount of scattering elements. These sections represent incompletely developed polycrystalline glacier ice containing firn inclusions. The increased amount of scatterers resulted in higher reflectivity of this area, referred to later in this study as “transition area” or ICE+FIRN. The changes in composition of glacier zones presented in Figure 2 are driven mainly by a continuous negative mass balance of Hansbreen.

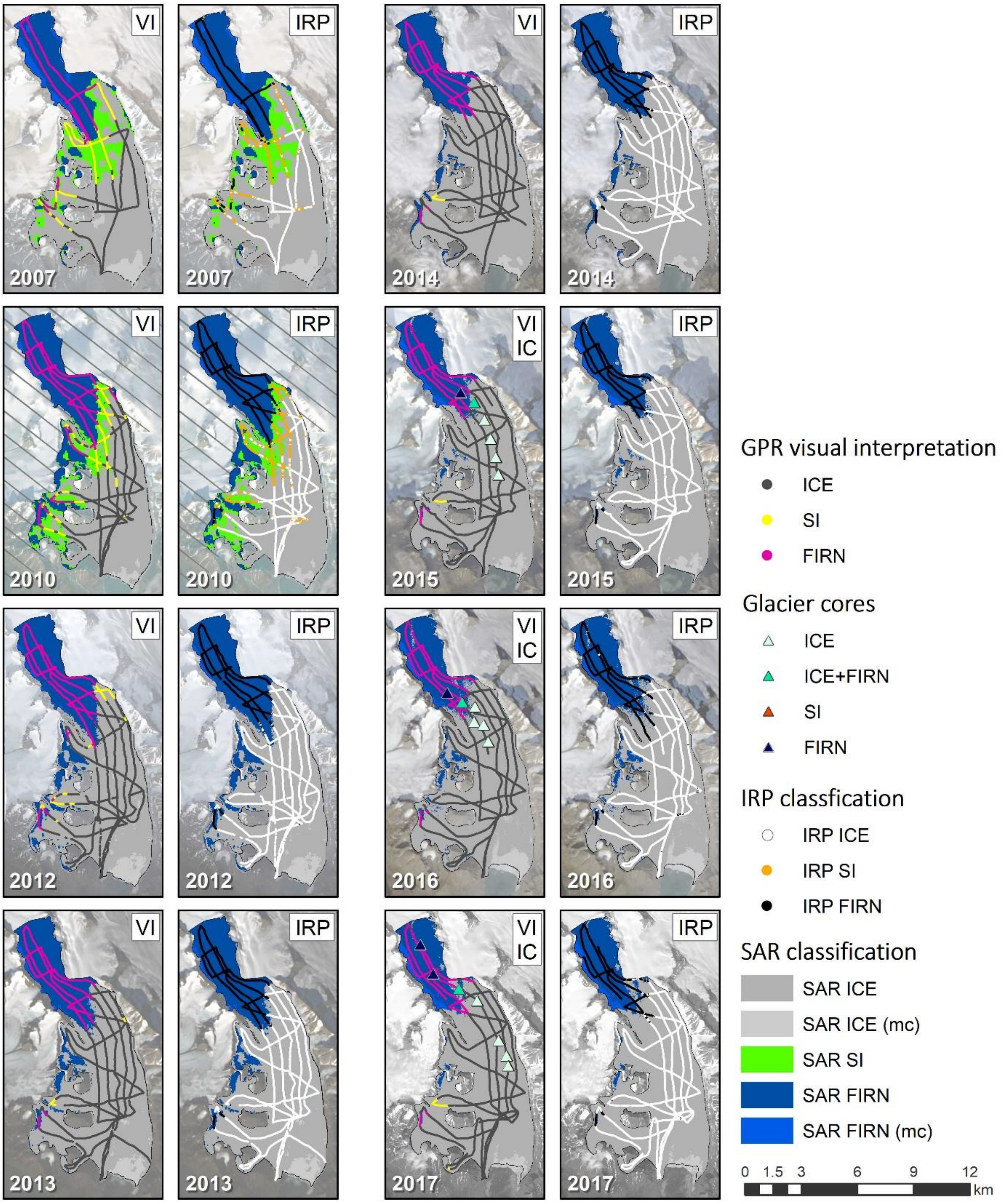

Figure 3a Results of GPR visual interpretation, glacier cores drilling, IRP and SAR classification on Hansbreen between 2007 and 2017 summer surface. GPR profiles excluded from analysis due to poor quality are not presented on the map plots. Abbreviation: mc – manually corrected. Background Landsat 7 and 8 images courtesy of the U.S. Geological Survey, Sentinel-2 images courtesy of the European Space Agency.

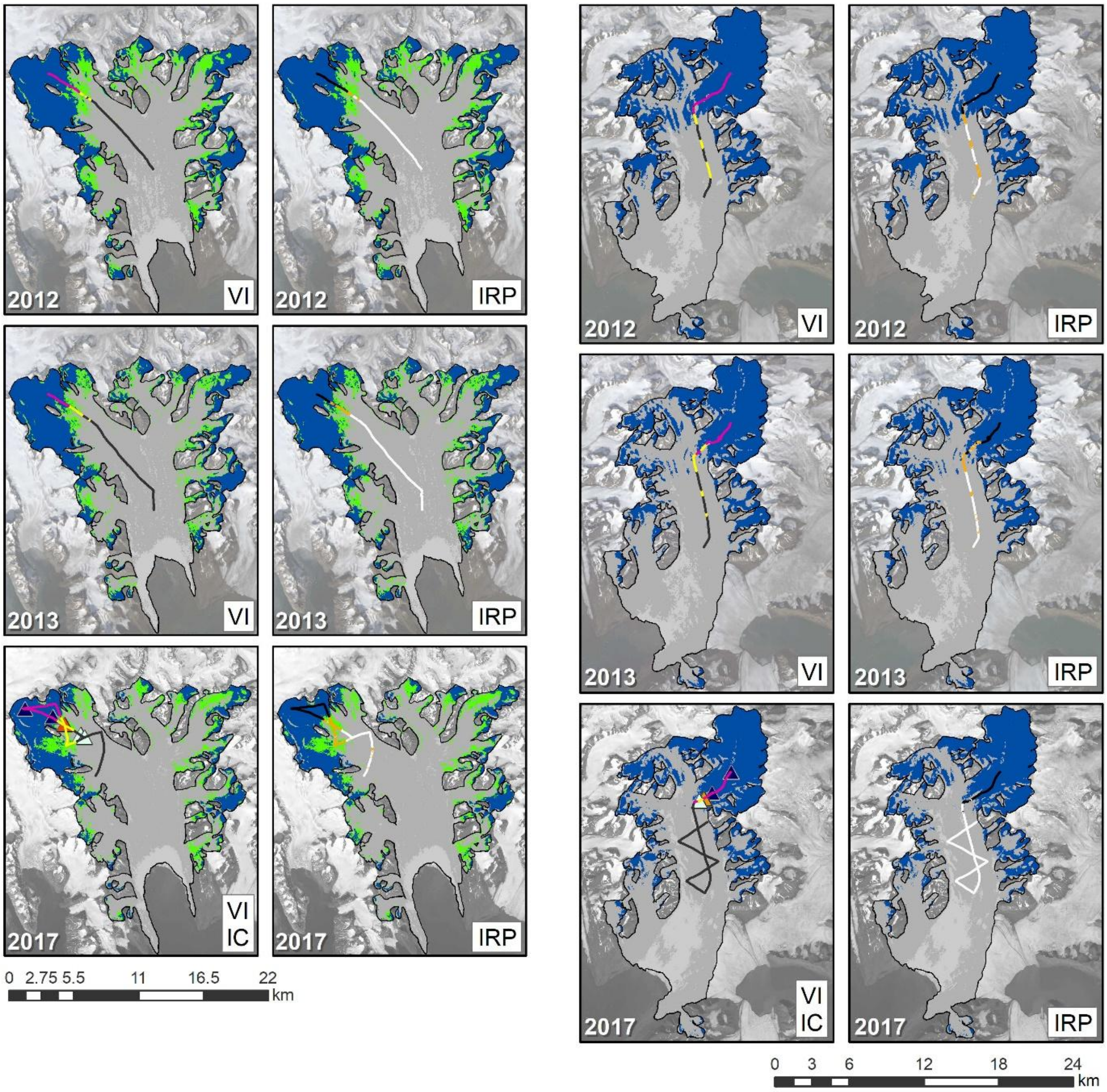

Figure 3b Results of GPR visual interpretation, glacier core drilling, IRP and SAR classification for Storbreen and Hornbreen between 2012 and 2017 summer surface. Legend is shown on Figure 3a. Background Landsat 7 and 8 images courtesy of the U.S. Geological Survey, Sentinel-2 images courtesy of the European Space Agency.

Figure 3a and 3b present the spatial location of classes derived from the GPR visual interpretation. In general, FIRN was detected in the GPR profiles covering the upper part of analysed glaciers, and SI (if present) was observed either directly below FIRN or as small sections of GPR data in between ICE or FIRN. ICE was classified on GPR profiles located mostly in the lower parts of glaciers. Both agreement of GPR visual interpretation results with typical location of glacier facies on a glacier and the homogeneity of distinguished classes on large areas demonstrated a high quality of performed GPR visual interpretation.

A distinct retreat of FIRN along GPR profiles can be observed on all analysed glaciers. Moreover, since 2016 on a GPR profile located in the top part of Hansbreen a short section of ICE is detected (Figure 3a). Additionally, since 2012, SI on Hansbreen was distinguished only on short sections of GPR profiles and its formation was mainly driven by a glacier's local topography. On Hornbreen, SI in 2012 and 2013 was detected both directly below FIRN on a GPR profile and as short sections between ICE or FIRN (Figure 3b). The location of the latter was determined by the topography of the glacier, whereas observed shrinkage of the local SI may be explained by Hornbreen's surface lowering (influencing glacier topography; Grabiec et al. 2017; Błaszczyk et al. 2019a) and a probable negative mass balance. In 2017 SI covered only 3% of GPR data from Hornbreen, but higher coverage of a glacier by GPR measurements could provide an answer if this SI was formed locally or as an extensive glacier zone. Unlike Hansbreen and Hornbreen, the SI of Storbreen covered a longer section of GPR profile in 2017 than in 2012 or 2013 (Figure 3b). This can be explained by the replacement of part of FIRN from 2014 by SI, the flatness of the glacier and the very low amount of crevasses on Storbreen. Therefore, a high amount of melted water froze on the glacier surface instead of migrating to the englacial system. The large contribution of meltwater ponds at the Storbreen surface has also been noticed on multispectral imagery in summer 2014 (Laska et al. 2017a).

5.2 SHALLOW GLACIER CORES

Cores retrieved from Hansbreen show very good agreement with results of GPR visual interpretation (Figure 3a and 3b). In the upper part of the glacier, FIRN was identified in all cores. For 2015, 2016 and 2017, summer surface cores of ice but with thin layers of firn were retrieved below the ELA. These cores were assigned to the transition area, where incompletely developed polycrystalline glacier ice occurs (symbolized as ICE+FIRN in Figure

3a). In the lower part of Hansbreen, cores of “blue” glacier ICE were retrieved, characterized by a rather homogeneous structure.

In the case of cores drilled in 2018 (i.e. related to the 2017 summer surface) on Storbreen, the agreement with GPR visual interpretation is also high. Two cores of FIRN were retrieved in the vicinity of the GPR profile indicating the presence of firn. Close to the crossing of GPR SI profiles, one core with SI was obtained. In the lower part of the glacier, two “blue” glacier ICE cores were retrieved, being in agreement with the GPR VI results.

Two FIRN cores, one from the upper part of Hornbreen, the second close to the ELA, were interpreted identically as GPR profiles for the 2017 summer surface. However, the core interpreted as SI was obtained in close proximity to the GPR section classified as FIRN, whereas the ICE core was obtained close to the SI GPR profile. The area of the drilling of the cores is where the tributary Isbroddbreen flows to Flatbreen and it is characterized by high elevation differences and thus local depressions in glacier topography. This could be a reason for disagreement in interpretation of these two cores and GPR. As an example, snow depth overlying the obtained ICE core was 2.37 m, whereas the same measure on a GPR profile in a point located close to the core drilling is estimated at 2.79 m. This suggests that the GPR profile was obtained along a local depression (filled by thicker snow cover), where at the end of the ablation season SI was formed, whereas the ICE core was retrieved in an elevated location – less favourable for superimposed ice formation. Although the position of GPR profiles was set based on accurate DGPS measurements, the location of the core drilling was set based on a simple handheld GPS device with an error of about 5 m. A similar situation could occur with the SI core retrieved in the vicinity of the GPR section of the thin FIRN area.

5.3 INTERNAL REFLECTION POWER

Internal Reflection Power (IRP) values of GPR profiles on every studied glacier were analysed (Figures 3a, 3b and 4). Figure 4 presents IRP along axes of Hansbreen, Storbreen and Hornbreen for every GPR dataset. In general, FIRN is represented by the highest values of IRP as a result of its strong reflectivity. Medium IRP values of SI are mainly an effect of scattering from high air bubble content of superimposed ice. The lowest IRP values represent ICE class due to the low amount of scatterers in the ice body. This pattern is in agreement with both analysis of GPR backscatter coefficient (Langley et al. 2007, 2008) and IRE (Grabiec 2017; Barzycka et al. 2019).

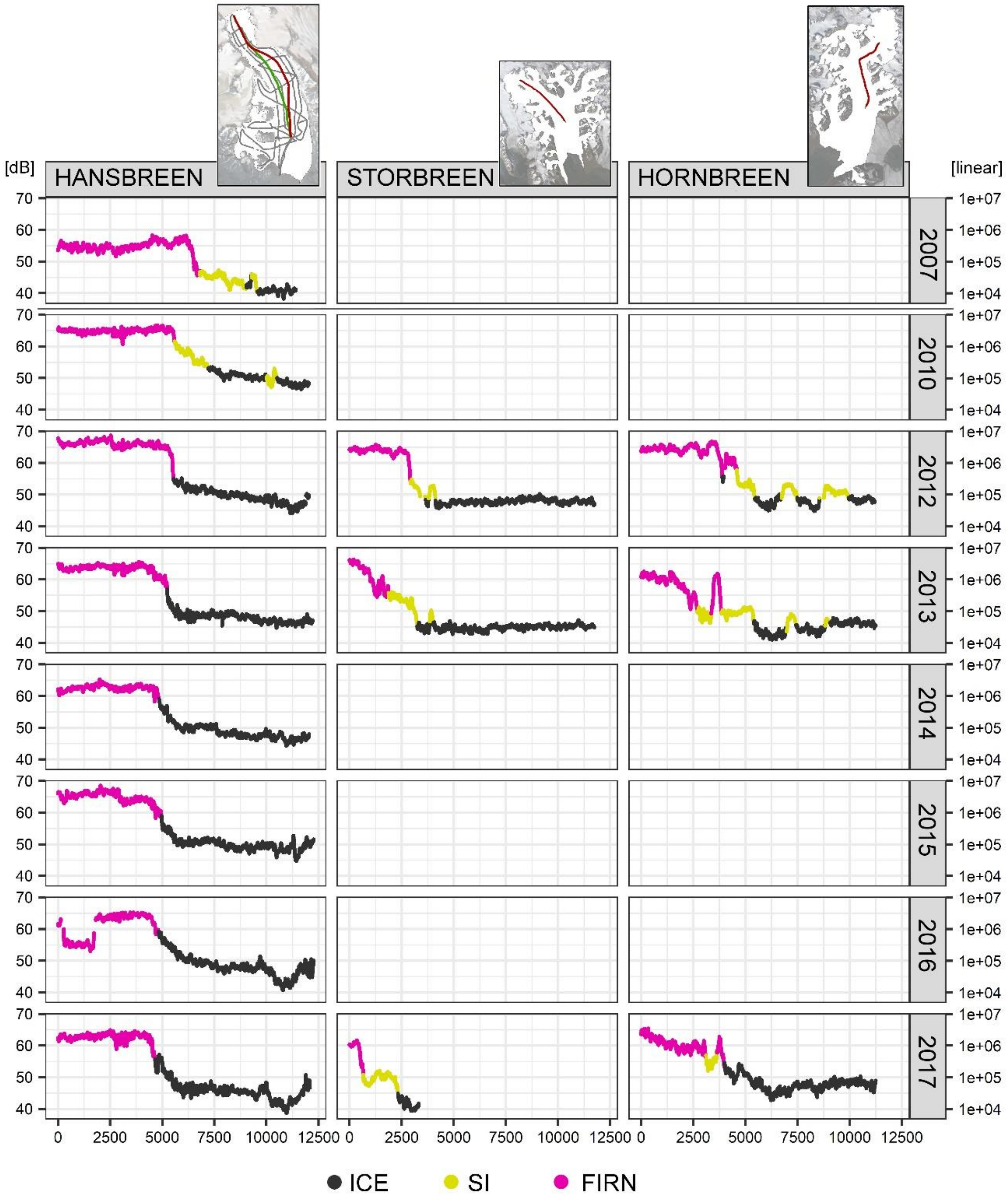

Figure 4 Internal Reflection Power along GPR profiles of axes of Hansbreen, Storbreen and Hornbreen of summer surfaces between 2007 and 2017. Colours on the graphs represent results of GPR visual classification. Please note that profile Hansbreen 2007 is located differently than Hansbreen 2010–2017, and thus separated by grey line and marked by green at Hansbreen's overview map.

Despite the overall agreement with the pattern of the IRP in relation to a glacier zone, a few exceptions and interesting artefacts can be observed. Firstly, in a profile of Hansbreen 2016 a rapid drop in IRP values representing FIRN occurs at a distance between 280 and 1730 m (Figure 4, Hansbreen 2016 segment). This section of the GPR profile was covered by a single GPR file, collected using a low-voltage battery. Despite pre-processing of the GPR dataset, the high noise recorded in the GPR file distinctly affected IRP values, resulting in an IRP drop of ca. 8 dB. Lower IRP values of FIRN also occur in e.g. the Storbreen and Hornbreeen 2013 datasets, close to the FIRN/SI boundary. In those sections of the GPR profiles, only a thin layer of FIRN was detected (less than 1 m), resulting in weaker scattering, moderate reflection and therefore lower IRP. In addition, the IRP values of ICE following FIRN class in profiles of Hansbreen 2016 and 2017 are characterized by a rather gentle decline, down to values around 50 dB. This gentle decrease of IRP is a result of noticeably higher scattering from a vast transition area of incompletely developed polycrystalline glacier ice. In addition, at ca. 9500 and 11 875 m of the Hansbreen 2016 and 2017 GPR profiles, a rapid peak of IRP values occurs. This is due to the presence of crevasses which are strong scatterers, influencing the IRP (a property described also by Copland and Sharp, 2011). Higher IRP values of ICE are also observed in Hornbreen datasets at distances starting from 10 000, 9100 and 8260 m for the 2012, 2013 and 2017 profiles of summer surfaces respectively and ending with the profiles. The increase in IRP is a result of the presence of crevasses, foliations and general low homogeneity of Hornbreen's ice body. This structure is a consequence of rather high velocity of the glacier and a surge episode in the past (Błaszczyk et al. 2013).

Similarly to plots of IRP values along the axes of the analysed glaciers, boxplots of IRP for all GPR datasets (Figure 5) also show distinct differences of IRP values between classes representing glacier zones. Boxes of IRP for ICE have the lowest values; in the middle boxes samples of SI are included (if present); upper boxes show IRP of FIRN class.

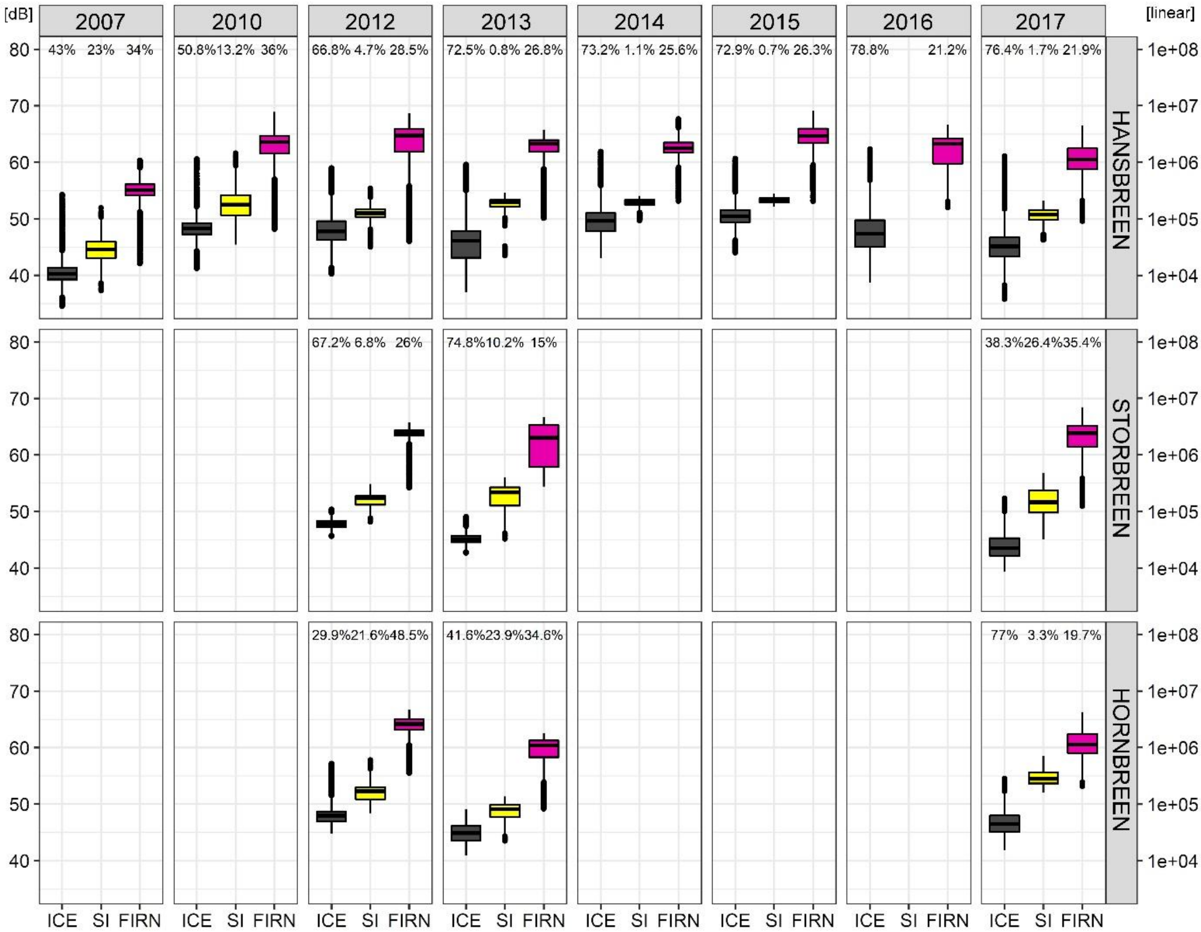

Figure 5 Boxplots of Internal Reflection Power for GPR datasets of Hansbreen, Storbreen and Hornbreen. The IRP values were grouped based on results of GPR visual interpretation. Boxplot symbols: solid horizontal line – median; horizontal lines of a box – first and third quantiles; vertical lines out of boxes – 1.5 interquantile range below and above first and third quantiles; dots – outliers.

Due to differences in settings of the GPR set during the GPR data collection, boxplot statistics of IRP – such as median or first and third quantiles of ICE, SI, FIRN – differ between GPR datasets. Nevertheless, datasets collected with the same settings (e.g. Hansbreen 2010, 2012, 2013 and 2016 datasets) demonstrate a similar pattern in the IRP distribution.

The difference in IRP between the upper quantile of ICE and lower quantile of SI is 2.8 dB on average. On the other hand, the average IRP difference between SI and FIRN is 8.0 dB.

Finally, the average IRP difference of the upper and lower quantiles of ICE and FIRN respectively equals 12.7 dB. The relatively small IRP difference of ICE and SI is mainly a result of median reflectivity of SI and often the presence of only a small thickness of superimposed ice layer formed on an ice body. FIRN, on the other hand, due to its generally high reflectivity is characterized by more distinct IRP than SI and ICE. It is worth noticing that in some GPR datasets SI is represented by only a few per cent of the total number of samples, so the SI statistics in the datasets may be distorted. Nevertheless, the IRP boxplots show a clear distinction between analysed glacier zones.

Generally, classification of IRP corresponds very well with results of visual interpretation of GPR profiles (Figure 3a and 3b). This is also expressed by high user's and producer's accuracies, F-score and Kappa (Table 3). The minimum Kappa is on a level of 0.85 (Hansbreen 2010 dataset) whereas the highest is 0.99 (Hansbreen 2013 and 2015, Storbreen 2012 datasets).

Table 3 Results of accuracy assessment of IRP natural breaks classification into three IRP classes: IRP ICE, IRP SI, IRP FIRN. Abbreviations: UA – user's accuracy, PA – producer's accuracy, F – F-score, K – Kappa.

		HANSBREEN				STORBREEN				HORNBREEN			
		UA	PA	F	K	UA	PA	F	K	UA	PA	F	K
2007	IRP ICE	0.90	0.92	0.91	0.90								
	IRP SI	0.79	0.78	0.79									
	IRP FIRN	0.97	0.96	0.97									
2010	IRP ICE	0.93	0.90	0.91	0.85								
	IRP SI	0.47	0.72	0.57									
	IRP FIRN	0.98	0.82	0.89									
2012	IRP ICE	0.90	1.00	0.95	0.93	0.99	1.00	0.99	0.99	0.94	0.94	0.94	0.96
	IRP SI	-	0.00	-		0.93	0.85	0.89		0.91	0.92	0.91	
	IRP FIRN	0.99	0.92	0.95		1.00	0.99	0.99		1.00	0.99	1.00	
2013	IRP ICE	0.99	1.00	0.99	0.99	0.98	1.00	0.99	0.94	0.92	0.95	0.93	0.91
	IRP SI	-	0.00	-		0.65	0.82	0.72		0.79	0.85	0.82	
	IRP FIRN	0.99	0.99	0.99		1.00	0.70	0.82		1.00	0.91	0.95	
2014	IRP ICE	0.98	0.99	0.99	0.98								
	IRP SI	-	0.00	-									
	IRP FIRN	0.97	1.00	0.98									
2015	IRP ICE	0.99	1.00	0.99	0.99								
	IRP SI	-	0.00	-									
	IRP FIRN	0.99	0.99	0.99									

2016	IRP ICE	1.00	0.95	0.97	0.96								
	IRP FIRN	0.85	0.99	0.91									
2017	IRP ICE	0.98	0.98	0.98	0.96	0.98	0.94	0.96	0.96	0.99	0.99	0.99	0.96
	IRP SI	-	0.00	-		0.89	0.98	0.93		-	0.00	-	
	IRP FIRN	0.92	0.99	0.95		1.00	0.98	0.99		0.86	1.00	0.92	

The extents of IRP FIRN are in good agreement with results of GPR VI (Figure 3a, 3b). Therefore, this class is characterized by high homogeneity and very good quality assessment results (average F-score: 0.95). On the other hand, the natural breaks classification of IRP was not successful in IRP SI distinction on Hansbreen 2012–2017 and Hornbreen 2017. This is due to the rather local character of superimposed ice represented by a small number of SI samples in these GPR datasets (see SI percentage in GPR datasets in Figure 5) which impeded a distinction of the IRP class representing SI. Due to the presence of only local SI, the accuracy of natural breaks classification in datasets where IPR SI was not distinguished was still high – the lowest Kappa of a dataset is 0.93 (Hansbreen 2012). In cases of successful IRP SI distinction (Hansbreen 2007, 2010; Storbreen; Hornbreen 2012, 2013) this class is also in good agreement with GPR VI, although less homogeneous than IRP FIRN. This is mostly a consequence of less distinct IRP values of SI than FIRN (Figure 5), therefore a misclassification mostly between IRP ICE and IRP SI occurs. Nevertheless, the average IRP SI F-score is on a level of 0.81 whereas that for IRP ICE is 0.96. The latter class also represents the glacier ice zone well, with few local noises of IRP SI or IRP FIRN class due to increase of IRP in e.g. crevassed areas.

A few exceptions to the otherwise very good representation of glacier zones by IRP classification are caused mainly by small thickness of a superimposed ice or firn layer and thus less intense scattering of the GPR signal. For example, thin SI on a western profile on Hansbreen 2007 was partly included in the IRP class representing ICE. This contributed significantly to lower PA (0.77) of IRP SI and UA (0.90) of IRP ICE. A similar situation occurred on Deileggbreen and Staszelisen (tributaries of Hansbreen) in 2010 and on Storbreen in 2013 where a thin layer of firn was partly included in the IRP SI class, lowering

PA of IRP SI to 0.47 and 0.65 respectively. On the other hand, a strong noise of GPR set due to low battery voltage in the Hansbreen 2016 dataset resulted in a lower threshold between IRP classes representing ICE and FIRN, affecting both spatial representation of the glacier zones and IRP FIRN's UA (0.85 versus ~0.98 for datasets of low SI contribution: Hansbreen 2013, 2014 and 2015). Finally, a small section of ICE in the upper part of the Hansbreen 2017 accumulation zone was not classified as IRP ICE, probably as a consequence of the moving average which smoothed the IRP to predominant IRP FIRN values in this section of the GPR profile.

5.4 SAR CLASSIFICATION

While Figure 3a and 3b presents results of SAR classification with superimposed GPR VI and GPR IRP classification, the results of SAR classification's accuracy assessment in reference to GPR visual interpretation are collected in Table 4.

Table 4 Results of accuracy assessment of SAR classification into three IRP classes: SAR ICE, SAR SI, SAR FIRN. Abbreviations: UA – user's accuracy, PA – producer's accuracy, F – F-score, K – Kappa.

		HANSBREEN				STORBREEN				HORNBREEN			
		UA	PA	F	K	UA	PA	F	K	UA	PA	F	K
2007	SAR ICE	0.76	0.96	0.85									
	SAR SI	0.61	0.49	0.54	0.80								
	SAR FIRN	1.00	0.80	0.89									
2010	SAR ICE	0.90	0.97	0.94									
	SAR SI	0.58	0.63	0.61	0.89								
	SAR FIRN	0.99	0.86	0.92									
2012	SAR ICE	0.92	0.98	0.95		0.96	0.99	0.98		0.56	0.97	0.71	
	SAR SI	-	0.00	-	0.93	0.65	0.62	0.64	0.95	-	0.00	-	0.76
	SAR FIRN	0.96	0.95	0.95		1.00	0.93	0.96		0.97	0.97	0.97	
2013	SAR ICE	0.98	0.99	0.98		0.94	1.00	0.97		0.60	1.00	0.75	
	SAR SI	-	0.00	-	0.98	0.84	0.29	0.43	0.92	-	0.00	-	0.73
	SAR FIRN	0.97	0.98	0.97		0.87	0.96	0.91		1.00	0.90	0.95	
2014	SAR ICE	0.97	1.00	0.98									
	SAR SI	-	0.00	-	0.97								
	SAR FIRN	1.00	0.95	0.97									
2015	SAR ICE	0.96	0.99	0.98									
	SAR SI	-	0.00	-	0.97								
	SAR FIRN	0.97	0.92	0.95									

2016	SAR ICE	0.98	0.99	0.98	0.98								
	SAR FIRN	0.95	0.94	0.94									
2017	SAR ICE	0.94	0.99	0.97	0.95	0.85	0.99	0.91	0.91	0.93	1.00	0.96	0.94
	SAR SI	-	0.00	-		0.89	0.74	0.81		-	0.00	-	
	SAR FIRN	0.98	0.85	0.91		1.00	0.94	0.97		0.97	0.86	0.91	

High coverage of Hansbreen by GPR measurements should ensure valid information on SAR classification's accuracy for this glacier. However, due to poor coverage of Storbreen and Horbreen by GPR measurements (as access to this area by a snowmobile is relatively difficult), their SAR classification's quality assessment results may, on the one hand, be strongly influenced by local misclassifications; on the other, they do not represent errors in other parts of the glaciers. Nevertheless, we believe that the GPR profiles crossing through all the glacier zones of Storbreen and Hornbreen along their main axes provide general information on SAR's classification accuracy.

The FIRN class is spatially very well represented in SAR classification results in all datasets (Figure 3a and 3b). This is reflected in the accuracy assessment results, where the average F-score of SAR FIRN for all datasets is 0.94. The lowest F-score of SAR FIRN is for Hansbreen 2007 and is mainly a result of misclassification of the firn area on tributary glaciers as SI. The misclassification was probably caused by the relatively low quality of the SAR dataset of three single HH polarization ENVISAT ASAR Wide Swath mode images of poor resolution. Another reason for the lower PA (and thus also F-score) of the SAR FIRN class is the depth of the firn layer. If thin, the total SAR backscattering value is also lower and the area may be classified as SAR SI or SAR ICE. For example, similarly to IRP classification, thin layers of FIRN on Deileggbreen and Staszelisen (Hansbreen 2010) were classified as SAR SI, partly causing the reduction of SAR FIRN's PA to 0.86. It is, however, worth mentioning that a SAR FIRN class occurs within no more than a few pixels of the GPR profile (Figure 3a).

Since 2014 and 2015 two small patches of SAR ICE have occurred in the eastern part of Hansbreen close to the ELA and have grown systematically from year to year. GPR profiles, on the other hand, were interpreted as FIRN till 2016. Results of GPR visual interpretation were in line with the IRP classification. Detailed analysis of the GPR profiles showed that a distinct loss of firn occurred at the GPR sections covering SAR ICE patches with a maximum loss of 2 m of firn between 2012 and 2013. In addition, ArcticDEM analysis shows that the SAR ICE patches are located in two local depressions. Therefore, the result of SAR classification as SAR ICE of those two areas since 2014 and 2015 could be a combination of less intense SAR signal scattering from thin firn and the influence of topography on SAR backscattering (Curlander and McDonough, 1991). This also influenced e.g. the PA of the Hansbreen 2016 and 2017 classification (0.94 and 0.85 respectively).

Results of the Hansbreen 2016 dataset SAR classification show characteristic SAR FIRN stripes along the ELA. This is a reflection of the transition area containing firn inclusions in glacier ice. The reason for the presence of more distinct stripes in SAR classification results of Hansbreen 2016 than of other SAR datasets may be: higher value of pixel spacing and resolution of analysed quad-polarimetric ALOS-2 PALSAR image (Table 1), lack of speckle filtering during ALOS-2 PALSAR pre-processing, higher quality of H–α Wishart classification in comparison to ISODATA+MLC or differences in penetration depth of L- and C-band SAR microwave (Barzycka et al. 2019). The presence of the transition area below the ELA was confirmed by shallow glacier cores collected for the 2015, 2016 and 2017 previous summer surface (Figure 3a) and lowered the UA of the Hansbreen 2016 SAR classification to 0.95.

Similarly to IRP, despite a high number of initial classes for the ISODATA classifier algorithm (later aggregated to SAR ICE, SAR SI, SAR FIRN), SAR SI of a local character was not distinguished (SAR datasets of Hansbreen 2012–2015, 2017). This may be explained by either a small depth of superimposed ice resulting in its penetration by a SAR signal or its insufficient representation by distinct backscattering values to form a separate class (partly also reduced by necessary SAR pre-processing). On the other hand, lack of a SAR SI class in results of Hornbreen’s classification is probably a consequence of high heterogeneity of its ice body. Natural scatterers in glacier ice – such as moraines or highly crevassed areas – produce higher SAR backscattering, reducing differences between glacier ice and superimposed ice SAR backscattering. This resulted in failure of SI SAR classification and lower Kappa of Hornbreen 2012 and 2013 (0.76 and 0.73 respectively) as SI was included in the SAR ICE class (SAR ICE UA at least 0.56, whereas PA = 0.97).

SAR classification of SI is highly dependent on superimposed ice thickness. For example, an area covered by the easternmost GPR profile in Hansbreen 2007 was classified as SAR ICE, whereas the GPR profile shows a thin layer of SI. Similarly to the SAR FIRN class in this dataset, SI on tributary glaciers was only partly correctly classified, probably due to the low quality of the SAR dataset. In addition, either small SI thickness, moving-window type SAR filtering (tendency of boundaries' displacements – König et al. 2004) or low SAR resolution was a reason for classification of SI close to the SI-ICE boundary as SAR ICE in the Hansbreen 2010 dataset (PA on 0.63 level) and Storbreen 2013 (PA on 0.29 level). The result of quality assessment of the latter was also influenced by another example of misclassification. Here, the GPR track crosses the centre of a wedge of FIRN area characterized by low thickness (max. 0.7 m, discussed also section 5.3). Due to less distinct backscattering of SI and thin FIRN, SAR filtering during pre-processing and low SAR resolution, some of the pixels along the GPR SI track following the FIRN wedge were classified as FIRN, lowering SAR SI's PA and FIRN's UA (0.89). Unfortunately, poor GPR coverage of Storbreen does not give us complete information on SAR classification performance on this glacier. Nevertheless, a relatively high F-score of SAR SI on Storbreen 2017 indicates improvement in SI classification thanks to higher resolution of the SAR dataset and better temporal coverage of the area by SAR (i.e. more SAR images in a dataset).

Although all SAR data were acquired during the ongoing accumulation season to take advantage of dry snow conditions, a SAR image from 1 March 2018 was characterized by lower backscattering values in the accumulation area of Hansbreen. This indicated water presence in the snowpack. Indeed, between 25 and 28 February 2018, positive temperatures and liquid precipitation were noted in the area (data from Hornsund station, eklima.no, The

Norwegian Meteorological Institute). This *rain-on-snow* event temporarily limited SAR penetration through the snowpack, resulting in lower values of SAR backscattering (Winsvold et al. 2018), which influenced the SAR classification results. As a consequence, based on the average SAR dataset of Hansbreen 2017, small parts of the FIRN area were classified as SAR ICE by ICODATA+MLC. This was carefully reclassified to SAR FIRN with the preservation of other artefacts such as a stipe of SAR ICE at the top of Hansbreen (a result of topographic conditions and negative mass balance). Similar low SAR backscattering was not noted on Storbreen or Hornbreen, probably due to preservation of dry snow conditions on this glacier prior to the SAR data acquisitions.

5.5 CHANGES OF GLACIER ZONES AND RELATION TO MASS BALANCE

Net mass balance gives information on the difference between accumulation and loss of glacier mass in a given season. On the other hand, firn and superimposed ice facies (represented here by SAR FIRN and SAR SI) build the accumulation zone of a glacier. Therefore changes in the accumulation area should be in strong relation to the mass balance of a glacier over a given time span. For analysis of glacier zones changes over time, maps and bar graphs of SAR glacier zones for Hansbreen, Storbreen and Hornbreen are presented (Figure 6). In addition, Table 5 contains the area of glacier zones in absolute and relative values for analysed SAR datasets as well as changes in glacier zones area for two time spans: 2007–2017 and 2012–2017.

Table 5 Area of glacier zones distinguished in SAR classification. "km^2" rows show area of each zone in km^2; "%" rows the percentage contribution of a zone to the glacier area; "Σarea [km^2]" rows the sum of glacier zones for a given year; whereas the "MB [m w.e.]" row contains information on Hansbreen's net mass balance in metres water equivalent from the WGMS database (WGMS 2019. Reference is given to the closing year of a mass balance season, e.g. mass balance for 2006/2007 is presented in the 2007 column). Differences in area and contribution for two reference time periods are presented in the "Δarea$_{17-07}$" and "Δarea$_{17-12}$" columns. The "Δzone$_{17-07}$" and Δzone$_{17-12}$" columns show the percentage loss/gain of zone area between 2007 and 2017 and between 2012 and 2017.

													Δ 2017-2007		Δ 2017-2012	
			2007	2008	2009	2010	2011	2012	2013	2014	2015	2016	2017	Δarea$_{17-07}$	Δzone$_{17-07}$	Δarea$_{17-12}$	Δzone$_{17-12}$
HANSBREEN	SAR FIRN	km^2	13.1			16.4		15.4	13.3	11.6	10.7	11.1	9.1	-4.0	-30.5%	-6.3	-40.9%
		%	25.6			32.0		30.2	26.3	23	21.3	22.3	18.4	-7.2		-11.8	
	SAR SI	km^2	7.1			7.2		0.0	0.0	0.0	0.0	0.0	0.0	-7.1	-100%		
		%	13.9			14.1		0.0	0.0	0.0	0.0	0.0	0.0	-13.9			
	SAR ICE	km^2	30.9			27.6		35.6	37.3	38.8	39.6	38.6	40.3	9.4	30.4%	4.7	13.9%
		%	60.5			53.9		69.8	73.7	77.0	78.7	77.7	81.6	21.1		11.8	
	Σarea [km^2]		51.1			51.2		51.0	50.6	50.4	50.3	49.7	49.4	-1.7	-3.3%	-1.6	-3.1%
	MB [m w.e.]		0.0	0.1	-0.8	0.0	-0.3	-0.2		-0.3	-0.4	-1.1	-0.7				
STORBREEN	SAR FIRN	km^2						55.5	51.5				35.1			-20.4	-36.7%
		%						28.5	26.6				18.6			-9.9	
	SAR SI	km^2						23.6	19.1				21.8			-1.8	-7.7%
		%						12.1	9.9				11.6			-0.6	
	SAR ICE	km^2						115.7	122.7				131.7			16.0	13.9%
		%						59.4	63.5				69.8			10.4	
	Σarea [km^2]							194.8	193.2				188.6			-6.2	-3.2%
HORNBREEN	SAR FIRN	km^2						67.1	53.8				51.1			-16.0	-23.8%
		%						39.0	31.4				30.2			-8.8	
	SAR ICE	km^2						105.0	117.3				118.3			13.3	12.7%
		%						61.0	68.6				69.8			8.8	
	Σarea [km^2]							172.1	171.1				169.4			-3.3	-1.9%

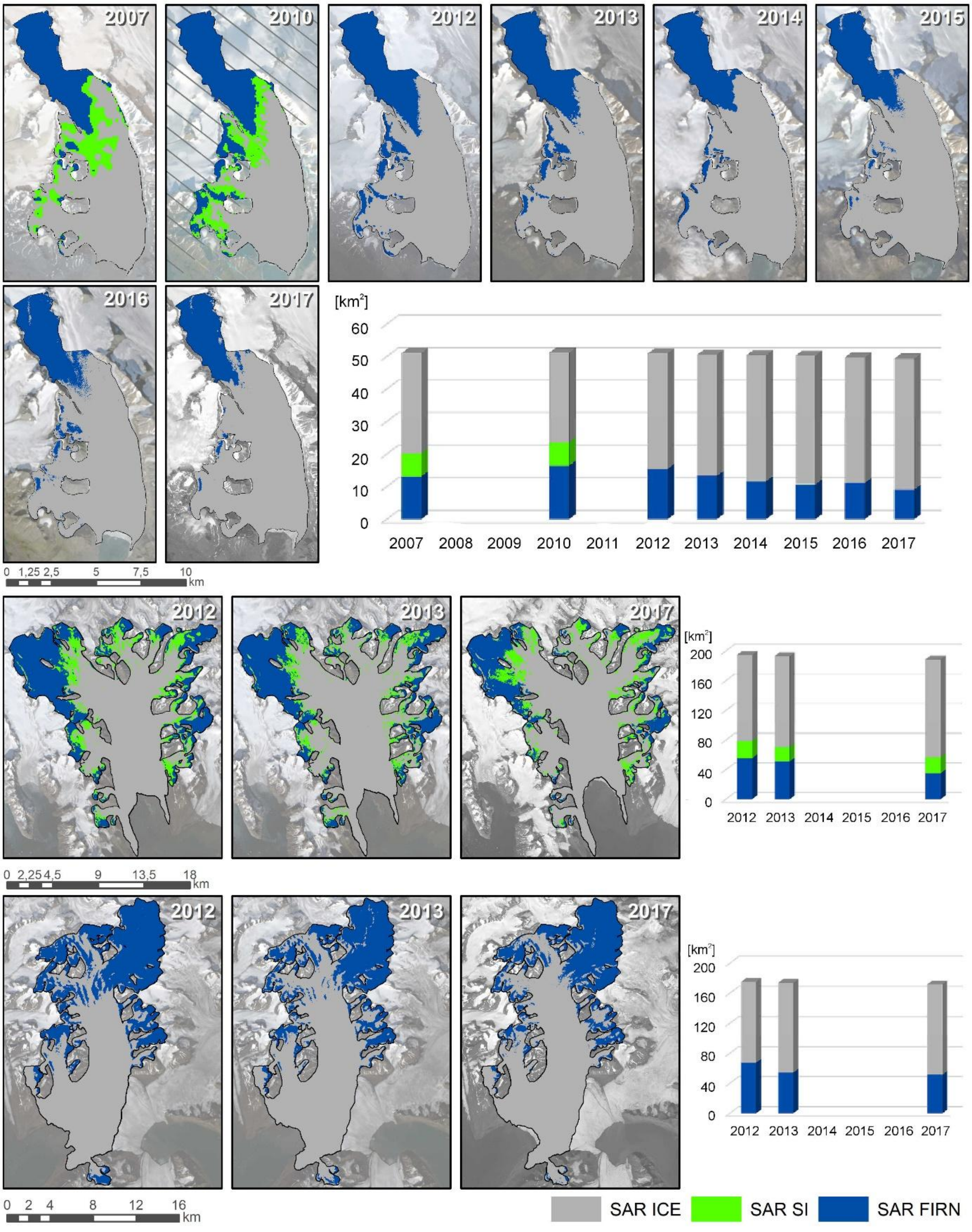

Figure 6 Results of glacier zones SAR classification with bar graphs showing changes of glacier zones for summer surface between 2007 and 2017 for Hansbreen and between 2012 and 2017 for Storbreen and Hornbreen.

Between 2007 and 2017, a significant loss of SAR FIRN is visible both on Hansbreen's main trunk and on its tributary glaciers (Figure 6). At the end of the 2007 ablation season it covered at least 13.1 km^2 (value significantly underestimated on tributary glaciers), reaching its maximum 16.4 km^2 at the end of the 2010 season. This increase of SAR FIRN area is a result of better performance of SAR classification on 2010 tributary glaciers and may also be related to positive/neutral mass balances in seasons 2007/2008 and 2009/2010 (Table 5). In the following years, SAR FIRN area on Hansbreen was decreasing until an increase of 1 km^2 between 2015 and 2016. As the mass balance for season 2015/2016 was strongly negative (−1.1 m w.e.), this increase of SAR FIRN area is rather unrealistic. Therefore, the gain of 1 km^2 of SAR FIRN between 2015 and 2016 is most likely caused by penetration capabilities of ALOS-2 PALSAR L-band or high resolution of the 2016 classification's results (in comparison to SAR C-band data). At the end of the 2017 ablation season, Hansbreen's SAR FIRN area was only 9.1 km^2. Therefore, between 2007 and 2017 Hansbreen lost at least 4.0 km^2 of SAR FIRN area, which equals 7.2% of its contribution to glacier area over this period. In addition, the SAR FIRN area covered 30.5% less area in 2017 than in 2007. The biggest cumulative loss, however, was noted between the 2010 and 2017 summer surface, i.e. when the SAR FIRN area was also distinguished on Hansbreen's tributary glaciers and when superficial net mass balance was constantly negative (2012/2013 net mass balance was excluded from the analysis as suspiciously positive – Błaszczyk et al. 2019b). The SAR FIRN loss for this period of time equalled 7.3 km^2, which is 13.6% of the contribution to the glacier area and 44.6% of SAR FIRN area shrinkage. This is mirrored in changes in spatial distribution of SAR FIRN (Figure 6) during the analysed period: the firn line on the main trunk of Hansbreen retreated and its asymmetry related to favourable western snow distribution (Grabiec et al. 2011; Laska et al. 2017b) is less evident. SAR FIRN on Hansbreen's tributary glaciers also covers significantly less area in 2017 than in 2010.

Between 2012 and 2017, the time period common to all analysed glaciers, Hansbreen lost 6.3 km^2 of SAR FIRN, corresponding to 11.8% of the contribution to glacier area and 40.9%

of SAR FIRN area loss. Higher values of the SAR FIRN relative changes for 2012–2017 than 2007–2017 indicate that the rate of SAR FIRN loss was more rapid in the former time span, as a response of the glacier to continuous negative mass balance after 2010. For the common 2012–2017 time span, the SAR FIRN area of Storbreen decreased by 20.4 km^2, which equals 9.9% of the contribution to total glacier area and 37.7% of SAR FIRN area loss. This is mirrored in the retreat of the firn line on all tributary glaciers of Storbreen (Figure 6). The smallest SAR FIRN area loss between 2012 and 2017 was recorded at Hornbreen (23.8%), with a decrease of contribution to total glacier area at the 8.8% level, which represents −16.0 km^2. The SAR FIRN loss is noticeable not only by retreat of the ELA but also by disappearance of the characteristic SAR FIRN patches in the upper part of Flatbreen, located in its surface depressions (also visible in the snow melting pattern during the ablation season, Laska et al. 2017a). It is worth mentioning that between 2012 and 2017 the biggest SAR FIRN area loss was noted on westernmost Hansbreen, whereas the lowest change occurred on easternmost Hornbreen. This is probably related to differences in local climatic conditions driven by the presence of the warm West Spitsbergen Current near the mouth of Hornsund Fiord and the cold East Spitsbergen Current on the Barents Sea side. This leads to air temperature gradient in the Hornsund basin, where higher temperature occurs in the western part of the basin, whereas the eastern part is typically colder (Vikhamar-Schuler et al. 2019), influencing glacier mass balance and changes of glacier zones extents.

SAR SI area for Hansbreen at the end of ablation seasons 2007 and 2010 was estimated to be at least 7 km^2 (~14% of the contribution to glacier area), whereas after 2010 this glacier zone was no longer detected. On Storbreen, SAR SI area for the end of the 2012 ablation season was estimated at 23.6 km^2 (12.1% of the glacier area) and 21.8 km^2 for 2017 (11.6% of the glacier area). This relatively small loss of SI (0.6% of the contribution to glacier area) can be explained by both underestimation of the SAR SI area for the 2010 season and advancement of SAR SI towards the upper part of the glacier in a place of previous SAR FIRN (Figure 6). Storbreen, as a glacier with low slope and small crevassed areas, has advantageous conditions for SI formation (Brandt et al. 2008). Although SAR SI was not detected on Hornbreen, results of GPR VI and GPR IRP classification (Figure 4b) show that the SI area on its main trunk decreased.

Table 6 Area of glacier zones of Hansbreen's main trunk distinguished by SAR classification. "SAR ACCUMULATION [km2]" row represents accumulation area, i.e. sum of SAR FIRN and SI. "MB [m w.e.]" row contains information on Hansbreen's superficial net mass balance in metres water equivalent from WGMS database (WGMS 2019. Reference is given to the year closing the mass balance season).

	2007	2008	2009	2010	2011	2012	2013	2014	2015	2016	2017
SAR FIRN [km^2]	12.1			12.8		12.5	11.5	10.4	10.1	9.8	8.7
SAR SI [km^2]	4.4			3.1							
SAR ICE [km^2]	21.6			22.5		25.7	26.3	27.2	27.4	27.2	28.0
SAR ACCUMULATION [km^2]	16.5			15.9	0.0	12.5	11.5	10.4	10.1	9.8	8.7
MASS BALANCE [m w.e.]	0.0	0.1	-0.8	0.0	-0.3	-0.2		-0.3	-0.4	-1.1	-0.7

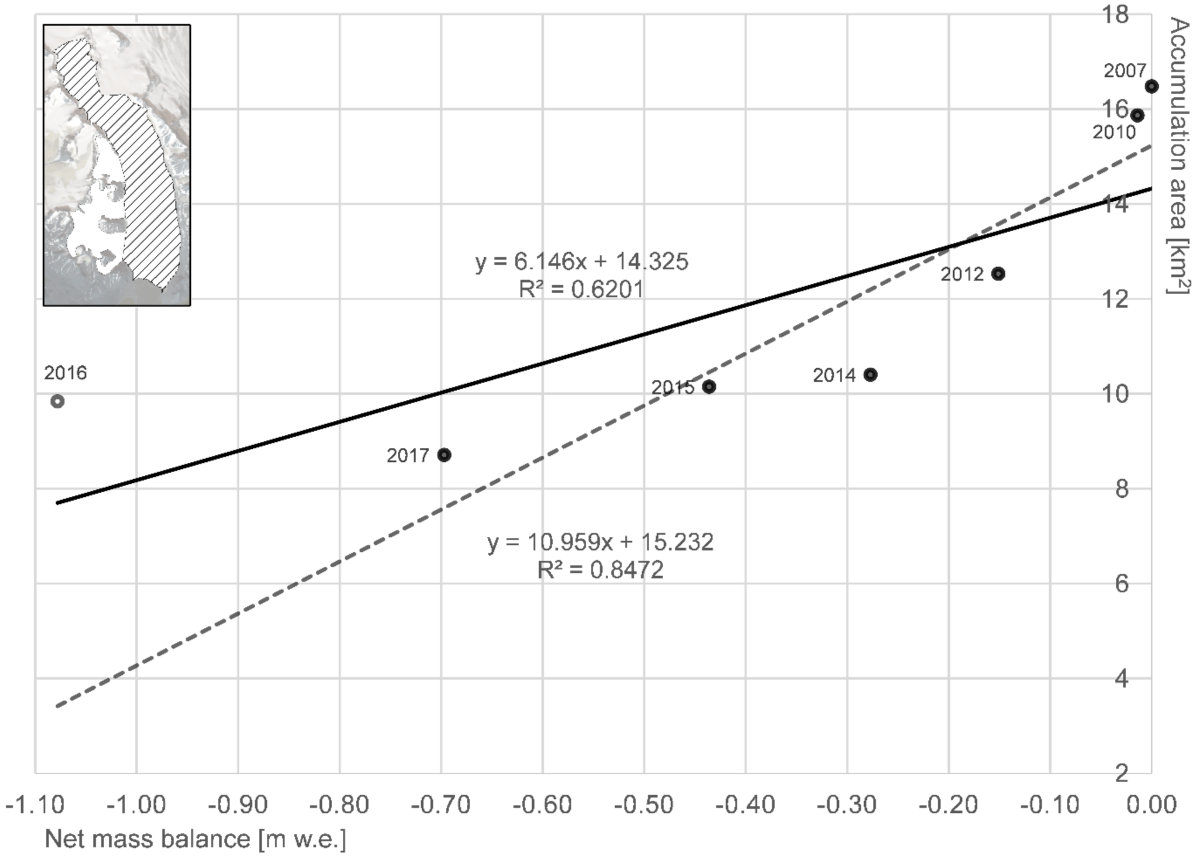

Figure 7 Superficial net mass balance and SAR accumulation area of Hansbreen's main trunk with trend lines. Solid line presents trend for 2007–2017 SAR accumulation area, whereas dashed line is a trend of data with the exception of 2016. Dashed area on overview map presents the main trunk of Hansbreen.

Relation of Hansbreen's superficial net mass balance and its SAR total accumulation area (Table 5) between 2007 and 2017 can be described by a correlation of 0.75. Although the correlation for this small number of observations is relatively strong, it is likely to be underestimated by misclassification of SAR FIRN and SI on tributary glaciers of Hansbreen 2007 as well as the increase of SAR FIRN area in Hansbreen 2016. In order to exclude an influence of misclassification of SAR FIRN and SAR SI for Hansbreen's tributary glaciers in 2007, a correlation coefficient between net mass balance and SAR accumulation area of only a main trunk of the glacier (Table 6; Figure 7) was calculated and equals 0.79. Similarly to König et al. (2004), due to a small number of observations the correlation coefficient is sensitive to misclassifications. For example, after excluding from analyses a rather unreal increase of accumulation area during the exceptionally negative mass balance season 2015/2016, the regression line is better fitted to the analysed data ($r = 0.92$, $r^2 = 0.85$; Figure 7). Therefore, although more observations are still needed, the analysed relation of mass balance and SAR accumulation area is promising for further studies of glacier zones in mass balance assessment contexts.

6 DISCUSSION

The very promising results of natural breaks classification of IRP show the possibility of applying it as an objective method of glacier facies discrimination from GPR data. Values of IRP significantly vary depending on the scattering properties of a medium, therefore IRP ICE, IRP SI and IRP FIRN classes have been retrieved with high agreement with GPR VI results. The main limitation of this method comes from the small thickness of a superimposed ice or firn layer and the poor representation of a glacier zone (up to several per cent of the GPR dataset). If a glacier zone is formed locally – and thus represented by a few samples of the GPR dataset – it is likely that it will be included in an IRP class represented by many samples. This could probably be resolved by applying IRP thresholds rather than natural breaks classification. However, the IRP absolute values are dependent on settings of GPR measurements and homogeneity of a glacier zone, therefore IRP thresholds should be carefully considered. Nevertheless, the IRP natural breaks classification is perfectly sufficient in regional-scale studies. For high-quality classification a moving time window for IRP calculation depending on snow depth is recommended, as it better represents thin layers of superimposed ice or firn than a fixed time window (Barzycka et al. 2019). Low-voltage batteries for the GPR set significantly affect IRP values, therefore they should be avoided, if possible, during field data collection.

The classification of SAR data acquired by sensors characterized by different bands, resolution or pixel spacing has given uneven but good results. Like the IRP classification, the possibility of discrimination of a class representing a glacier zone is highly dependent on the thickness and representation of a glacier structure. In addition, the accurate representation of glacier facies by SAR classes is dependent on SAR data capacity, such as polarimetry level, resolution or pixel spacing. This is especially valid for superimposed ice, which on analysed glaciers was often thin, therefore SAR signal scattering was not as distinct as for highly scattered – and thus well-represented – firn. Nevertheless, good results of SAR SI classification based on high-quality Sentinel-1 data for Storbreen 2017 are very promising for future studies.

The ISODATA+MLC method is not recommended for SI detection on glaciers with a presence of vast, highly crevassed areas which – as strong SAR scatterers – impede SAR SI classification. This influence of the glacier ice heterogeneity on SAR classification results may be reduced by modern, high-quality SAR sensors. However, due to poor coverage of GPR on Hornbreen, it is difficult to know whether non-detection of SAR SI for the 2017 modern Sentinel-1 SAR dataset was due to the vast crevassed areas or the local character of SI. It is possible that the discrimination of glacier zones with analysis of quad-polarimetric SAR data and algorithms such as H–α Wishart would be able to detect SI on Hornbreen. However, this kind of data and method was not analysed in Hornbreen's case in this study.

One of many indicators of climate change in the Hornsund fiord basin is an increased frequency of winter rains (Łupikasza et al. 2019). If a winter rain or melting event occurs, the snowpack is temporarily characterized by higher liquid water content, resulting in significantly lower SAR backscattering. Even one image in a SAR stack, where the wet snow conditions are mirrored, may influence SAR classification of glacier facies. Therefore, it is recommended that meteorological data for days of SAR image acquisition as well as several days prior to the acquisition be examined, as due to the percolation process in a snowpack the SAR signal attenuation is prolonged (Winsvold et al. 2018). In this study, no influence of ice layers in the snowpack on SAR classification results was found.

The maximum loss of SAR FIRN area on Hansbreen for the analysed 2007–2017 time span was recorded between 2010 and 2017 and equalled 13.6% of the contribution to glacier area. Before that period the net mass balance of Hansbreen fluctuated between positive, neutral and negative. After 2010 however, it was constantly negative, resulting in a constant decrease of the SAR FIRN zone area. For a time span common for all datasets, i.e. 2012–2017, Hansbreen recorded the biggest percentage SAR FIRN area loss and its contribution to glacier total area, Storbreen recorded a medium loss of SAR FIRN and its contribution to glacier area, whereas Hornbreen recorded the smallest changes among the analysed glaciers. This decrease of relative SAR FIRN loss from the westernmost to the easternmost glacier can be explained by temperature gradient driven by the warm West Spitsbergen Current and cold East Spitsbergen Current – strong factors shaping local climate (Vikhamar-Schuler et al. 2019) and, in consequence, e.g. glaciers' mass balance or changes in glacier zones.

Storbreen is the only one of the three analysed glaciers where the vast area of the SAR SI zone was detected at the end of the study period. This is most likely due to Storbreen's favourable conditions for superimposed ice formation such as topography and drainage pattern. Due to failure in SAR SI distinction on Hornbreen, it is impossible to say how this zone has changed over time. However, based on results of GPR VI and IRP classification from 2012, 2013 and 2017, a decrease of SI along the glacier axis can be observed. SAR SI of Hansbreen covered at least 7 km^2 in 2007 and 2010, and since 2012 has not been distinguished as a vast area. This is probably a consequence of negative mass balance, changes in the glacier topography (Błaszczyk et al. 2019a) and the effective drainage system of Hansbreen (Decaux et al. 2019).

Dunse et al. (2009) observed an increase in firn area extent of Austfonna between the 2003 and 2006 summer surface. König et al. (2004), for the 1992–2003 time span, reported a stable location of Kongsvegen's firn line until 1999, when larger negative mass balance was noted, resulting in a retreat of the firn line. In consequence ca. 8% less contribution of firn zone to the glacier's area was noted. For the same glacier, but in a different time span (2009–2016), Winsvold et al. (2018) described a stable position of the firn line along the glacier's main axis. It is difficult to compare directly the results of this study with examples of glacier facies monitoring from Svalbard, as they either cover a different time span (König et al. 2004; Dunse et al. 2009) or are focused on highly temporal changes along the glacier's main axis (Winsvold et al. 2018). However, based on the above, we might conclude that changes of glacier zone extent in Hornsund are rather significant.

A strong relationship has been found between changes in the SAR accumulation area of Hansbreen's main trunk and its superficial net mass balance. This is especially true for observations excluding the 2016 season, for which the SAR FIRN area was likely to be overestimated and also exceptionally negative mass balance was noted. The strong relationship between SAR zones and the mass balance of Hansbreen fits with the results of Engeset et al. (2002) and König et al. (2004) where a strong correlation between the mass balance of Kongsvegen and glaciers in the vicinity and either the ELA or firn area was described.

The number of analysed observations of SAR accumulation area and Hansbreen's mass balance is small, therefore the calculated correlation coefficients should be carefully considered. In the future, longer series of observations will allow the regression model of Hansbreen's net mass balance and accumulation area to be updated and improved. In addition, based on the model and information on relative differences of accumulation areas' loss between Hansbreen, Strobreen and Hornbreen it might be possible to assess the mass balance of Storbreen and Hornbreen, as an alternative to the lack of continuous glaciological monitoring in the inner part of the Hornsund basin area.

7 CONCLUSIONS

This study has examined changes of the glacier zones of Hansbreen, Storbreen and Hornbreen, located in the Hornsund fiord basin, between the 2007 and 2017 summer surfaces. The analysis is based on both SAR and *in situ* data (i.e. cores and GPR measurements). A novel application of the IRP coefficient has been tested as an alternative method to GPR visual interpretation. The main findings of this research are as follows:

- Internal Reflection Power coefficient varies depending on the scattering mechanism of the medium, i.e. glacier zone. Due to its objectivity, simplicity and high accuracy, the IRP natural breaks classification method is highly recommended for future studies of glacier facies based on GPR data. The main limitation of IRP classification by natural breaks algorithm comes from the thickness of SI of the firn layer and representation of a glacier zone.
- SAR classification gave good results. Limitations of the applied methods are related mainly to: (1) thickness and representation of a glacier zone, (2) heterogeneity of glacier ice, (3) quality of SAR data. Due to a strong and distinct scattering mechanism, the firn zone is characterized by the highest classification accuracy. Very good results of SAR classification based on modern, out-of-charge Sentinel-1 SAR data are very promising for the future study of glacier zones.
- The maximum loss of SAR FIRN area on Hansbreen for the analysed 2007–2017 time span was recorded between 2010 and 2017 and equalled 13.6% of the contribution to glacier area (44.5% of SAR FIRN's area loss).
- For a common time span of analysis (i.e. 2012–2017), the westernmost glacier, Hansbreen, recorded the largest percentage loss of SAR FIRN area (40.9%),

Storbreen the medium loss (36.7%), and Hornbreen, the easternmost glacier, the smallest loss (23.8%). The same pattern applies to the loss of SAR FIRN contribution to the total glacier area (Hansbreen: −11.8%, Storbreen: −9.9%, Hornbreen: −8.8%). This east-to-west gradient of loss in the firn zone areas is probably related to local climatic conditions shaped by the East and West Spitsbergen Currents.

- The SAR SI zone on Hansbreen covered at least 7 km^2 in 2007 and 2010, and since 2012 SI has formed only locally. Due to favourable topographic conditions, SI is formed on Storbreen as a vast zone, covering around 11% of its area including locations where SAR FIRN was present in previous seasons.
- Correlation between the SAR accumulation zone of Hansbreen's main trunk and its net mass balance has been found to be strong but – due to the small number of observations – very sensitive to misclassifications. The estimated 0.92 correlation coefficient (coefficient of determination: 0.85) is very promising for future studies of mass balance assessments of glaciers located in the Hornsund fiord basin, but more observations are recommended to better describe the mass balance model.

FUNDING

This work was primarily supported by the Centre for Polar Studies (the Leading National Research Centre in Earth Sciences for 2014-2018) funding, No. 03/KNOW2/2014. The field data collection and/or processing received grant aid from: the National Centre for Research and Development within the Polish-Norwegian Research Cooperation Programme (AWAKE2 project Pol Nor/198675/17/2013), Polish-Norwegian funding (AWAKE project PNRF-22-AI-1/07), Polish Ministry of Science and Higher Education (GLACJODYN No. IPY/269/2006), Polish National Centre for Research and Development (SvalGlac project No. NCBiR/PolarCLIMATE-2009/2-2/2010), European Union 7th Framework Programme (ice2sea programme, grant no. 226375, contribution no. 108) and the Research Council of Norway (Arctic Field Grant 2018 No. 282538, RiS ID: 10917). Glaciological data were processed under assessment of the University of Silesia data repository within project Integrated Arctic

Observing System (INTAROS, European Union’s Horizon 2020 research and innovation programme – grant No. 727890). The European Space Agency (Third Part Missions Project ID: 40201) provided RADARSAT-2 data.

ACKNOWLEDGEMENTS

Authors would like to thank all members of University of Silesia’s scientific expeditions to Hornsund who helped with field data collection as well as wintering crews of Polish Polar Station in Hornsund for their hospitality and assistance.

CONTRIBUTION

Barzycka B. implemented the project, analysed SAR, IRP, changes of glaciers zones and wrote the manuscript. Grabiec M. preformed GPR visual interpretation and wrote 3.2 and 4.1 chapters of the paper. Grabiec M., Jania J. and Barzycka B. conceptualized and/or developed an IRP application. Grabiec M., Ignatiuk D., Laska M. and Barzycka B. provided GPR and/or glacier cores data. Błaszczyk M. supported manual correction of SAR classification results and provided glaciers outlines. Jania J. and Hagen J. O. supported glaciological part of this study and the implementation of the research. All authors provided critical feedback and helped shape the research, analysis and manuscript.

Conflicts of Interest: The authors declare no conflict of interest.

REFERENCES

Akbari, V., Doulgeris, A. P., & Eltoft, T. (2014) Monitoring Glacier Changes Using Multitemporal Multipolarization SAR Images. *IEEE Transactions on Geoscience and Remote Sensing, 52*(6), 3729-3741. DOI: 10.1109/TGRS.2013.2275203

Baird, P. (1952). Part I: Method of Nourishment of the Barnes Ice Cap. *Journal of Glaciology, 2*(11), 2-9. DOI: 10.3189/S0022143000025910

Ball, G. H. & Hall, D. J. (1965) *ISODATA, a Novel Method of Data Analysis and Pattern Classification*. (Report No. AD 699616) Menlo Park, CA: Stanford Research Institute.

Barzycka, B., Błaszczyk, M., Grabiec, M. & Jania, J. (2019). Glacier facies of Vestfonna (Svalbard) based on SAR images and GPR measurements. *Remote Sensing of Environment, 221*, 373–385. DOI: 10.1016/j.rse.2018.11.020.

Benson, C. S. (1961) Stratigraphic studies in the snow and firn of the Greenland ice sheet. *Folia Geographica Danica, 9*, 13-37.

Błaszczyk, M. (2012) Porównanie możliwości identyfikacji stref lodowców na podstawie obrazów radarowych ERS SAR oraz ALOS PALSAR [Capability of Glacier Zone Detection Using Radar Images - ERS SAR and ALOS PALSAR] *Archiwum Fotogrametrii, Kartografii i Teledetekcji, 24*, 21-30.

Błaszczyk, M., Jania, J. A. & Kolondra, L. (2013). Fluctuations of tidewater glaciers in Hornsund Fjord (Southern Svalbard) since the beginning of the 20th century. *Polish Polar Research, 34*(4), 327-352. DOI: 10.2478/popore-2013-0024

Błaszczyk, M., Ignatiuk, D., Grabiec, M., Kolondra, L., Laska, M., Decaux, L., Jania, J., Berthier, E., Luks, B., Barzycka, B. & Czapla, M. (2019a). Quality Assessment and Glaciological Applications of Digital Elevation Models Derived from Space-Borne and Aerial Images over Two Tidewater Glaciers of Southern Spitsbergen. *Remote Sensing, 11*(9), 1121. DOI: 10.3390/rs11091121

Błaszczyk, M., Ignatiuk, D., Uszczyk, A., Cielecka-Nowak, K., Grabiec, M., Jania, J. A., Moskalik, M. & Walczowski, W. (2019b). Freshwater input to the Arctic fjord Hornsund (Svalbard). *Polar Research, 38*. DOI: 10.33265/polar.v38.3506

Boetius, A., Anesio, A., Deming, J., Mikucki, J. A. & Rapp, J. Z. (2015) Microbial ecology of the cryosphere: sea ice and glacial habitats. *Nature Reviews Microbiology, 13*, 677–690. DOI: 10.1038/nrmicro3522

Bourbiguot, M., Johnsen, H. & Piantanida, R. (2016) *Sentinel-1 Product Definition* (Report No. S1-RS-MDA-52-7440). Retrieved from the European Space Agency: Sentinel Online website: https://sentinel.esa.int/documents/247904/1877131/Sentinel-1-Product-Definition

Brandt, O., Kohler, J. & Lüthje, M. (2008) Spatial mapping of multi-year superimposed ice on the glacier Kongsvegen, Svalbard. *Journal of Glaciology, 54*(184), 73-80. DOI: 10.3189/002214308784409080

Braun, M. & Hock, R. (2004) Spatially distributed surface energy balance and ablation modelling on the ice cap of King George Island (Antarctica). *Global and Planetary Change, 42*, 45-58. DOI: 10.1016/j.gloplacha.2003.11.010

Catania, G., Conway, H., Gades, A., Raymond, C., & Engelhardt, H. (2003). Bed reflectivity beneath inactive ice streams in West Antarctica. *Annals of Glaciology, 36*, 287-291. DOI: 10.3189/172756403781816310

Caves, R. & Williams, D. (2015) *Geolocation of RADARSAT-2 Georeferenced Products.* (Report No. RN-TN-53-0076). Richmond, B.C.: MacDonald, Dettwiler and Associates Ltd.

Cloude, S.R. & Pottier, E. (1996) A review of target decomposition theorems in radar polarimetry. *IEEE Transactions on Geoscience and Remote Sensing, 34*(2), 498-518. DOI: 10.1109/36.485127

Cloude, S.R. & Pottier, E. (1997) An entropy based classification scheme for land applications of polarimetric SAR. *IEEE Transactions on Geoscience and Remote Sensing, 35*(1), 68-78. DOI: 10.1109/36.551935

Copland, L., & Sharp, M. (2001). Mapping thermal and hydrological conditions beneath a polythermal glacier with radio-echo sounding. *Journal of Glaciology, 47*(157), 232-242. DOI: 10.3189/172756501781832377 de Smith, M. J., Goodchild, M. F. & Longley, P. (2007). Geospatial Analysis: A Comprehensive Guide to Principles, Techniques and Software Tools. 2nd edition. Troubador Publishing Ltd. ISBN: 978-1906221522

Curlander, J. C. & McDonough R. N. (1991) *Synthetic Aperture Radar: Systems and Signal Processing*. Hoboken, NJ: John Wiley & Sons. 647 pp. ISBN: 978-0-471-85770-9.

Decaux, L., Grabiec, M., Ignatiuk, D. & Jania, J. (2019) Role of discrete water recharge from supraglacial drainage systems in modeling patterns of subglacial conduits in Svalbard glaciers*. The Cryosphere, 13*, 735-752. DOI: 10.5194/tc-13-735-2019

Doornbos, E., Scharroo, R., Klinkrad, H., Zandbergen, R. & Fritsche, B. (2002) Improved modelling of surface forces in the orbit determination of ERS and ENVISAT. *Canadian Journal of Remote Sensing, 28*(4), 535-543, DOI: 10.5589/m02-055

Dunse, T., Schuler, T., Hagen, J., Eiken, T., Brandt, O. & Høgda, K. (2009). Recent fluctuations in the extent of the firn area of Austfonna, Svalbard, inferred from GPR. *Annals of Glaciology, 50*(50), 155-162. DOI: 10.3189/172756409787769780

Dyurgerov, M., Meier, M., & Bahr, D. (2009). A new index of glacier area change: A tool for glacier monitoring. *Journal of Glaciology, 55*(192), 710-716. DOI: 10.3189/002214309789471030

Engeset, R. V., Kohler, J., Melvold, K. & Lundén, B. (2002) Change detection and monitoring of glacier mass balance and facies using ERS SAR winter images over Svalbard. *International Journal of Remote Sensing, 23*(10), 2023-2050, DOI: 10.1080/01431160110075550

Environmental Systems Research Institute, (2017). *Iso Cluster*. Retrieved from: ArcGIS Desktop Help 10.5 Spatial Analyst website: https://desktop.arcgis.com/en/arcmap/10.5/tools/spatial-analyst-toolbox/iso-cluster.htm

Gacitúa, G., Uribe, J., Wilson, R., Loriaux, T., Hernández, J. & Rivera, A. (2015). 50 MHz helicopter-borne radar data for determination of glacier thermal regime in the central Chilean Andes. *Annals of Glaciology, 56*(70), 193-201. DOI: 10.3189/2015AoG70A953

Gades, A., Raymond, C., Conway, H. & Jagobel, R. (2000). Bed properties of Siple Dome and adjacent ice streams, West Antarctica, inferred from radio-echo sounding measurements. *Journal of Glaciology, 46*(152), 88-94. DOI: 10.3189/172756500781833467

Ganju, N. K., Defne, Z., Kirwan, M.L., Fagherazzi, S., D'Alpaos, A. & Carniello, L. (2017) Spatially integrative metrics reveal hidden vulnerability of microtidal salt marshes. *Nature Communications. 8*, 14156. DOI: 10.1038/ncomms14156

Grabiec, M., Leszkiewicz, J., Głowacki, P. & Jania, J. (2006). Distribution of snow accumulation on some glaciers of Spitsbergen. *Polish Polar Research, 27*(4), 309-326.

Grabiec, M., Puczko, D., Budzik, T., & Gajek, G. (2011). Snow distribution patterns on Svalbard glaciers derived from radio-echo soundings. *Polish Polar Research, 32*(4), 393-421. DOI: 10.2478/v10183−011−0026−4

Grabiec, M., Jania, J., Puczko, D., Kolondra, L., & Budzik, T. (2012). Surface and bed morphology of Hansbreen, a tidewater glacier in Spitsbergen. Polish Polar Research, 33(2), 111-138. DOI: 10.2478/v10183-012-0010-7

Grabiec, M. *Stan i Współczesne Zmiany Systemów Lodowcowych Południowego Spitsbergenu w Świetle Badań Metodami Radarowymi (The State and Contemporary Changes of Glacial Systems in Southern Spitsbergen in the Light of Radar Methods)*; Wydawnictwo Uniwersytetu Śląskiego: Katowice, Poland, 2017; p. 328. ISBN 978-83-226-3015-0.

Grabiec, M., Ignatiuk, D., Jania, J. A., Moskalik, M., Głowacki, P., Błaszczyk, M., Budzik, T. & Walczowski, W. (2018) Coast formation in an Arctic area due to glacier surge and retreat:

The Hornbreen–Hambergbreen case from Spistbergen. *Earth Surface Processes and Landforms, 43*, 387– 400. DOI: 10.1002/esp.4251

Hagen, J. O., Kohler, J., Melvold, K. & Winther, J. G. (2003) Glaciers in Svalbard: mass balance, runoff and freshwater flux. *Polar Research, 22*, 145-159. DOI: 10.1111/j.1751-8369.2003.tb00104.x

Hall, D., Ormsby, J., Bindschadler, R. & Siddalingaiah, H. (1987) Characterization of Snow and Ice Reflectance Zones On Glaciers Using Landsat Thematic Mapper Data. *Annals of Glaciology, 9*, 104-108. DOI: 10.3189/S0260305500000471

Hall, D. K. (1996) Remote sensing applications to hydrology; imaging radar. *Hydrological Sciences Journal, 41*(4), 609-624, DOI: 10.1080/02626669609491528

Hall, D. K., Foster, J. L., Verbyla, D. L., Klein, A. G. & Benson, C. S. (1998) Assessment of Snow-Cover Mapping Accuracy in a Variety of Vegetation-Cover Densities in Central Alaska. *Remote Sensing of Environment, 66*(2), 129-137. DOI: 10.1016/S0034-4257(98)00051-0

Harris, B. (1998) *Envisat Mission, Product Summary Overview*. AG Noordwijk: ESA Publications Division. ISBN 92-9092-480-2.

Hodson, A., Anesio, A. M., Tranter, M., Fountain, A., Osborn, M., Priscu, J., Laybourn-Parry, J. & Sattler, B. (2008), Glacial Ecosystems. *Ecological Monographs, 78*, 41-67. DOI: 10.1890/07-0187.1

Hoffman, M. J., Fountain, A. G. & Liston, G. E. (2008) Surface energy balance and melt thresholds over 11 years at Taylor Glacier, Antarctica. *Journal of Geophysical Research, 113*(F04014). DOI: 10.1029/2008JF001029.

Ignatiuk, D., Piechota, A., Ciepły, M. & Luks, B. (2014) Changes of Altitudinal Zones of Werenskioldbreen and Hansbreen in Period 1990 – 2008, Svalbard. *AIP Conference Proceedings, 1618*(1), 275-280. DOI: 10.1063/1.4897727

Jania, J., Macheret, Y., Navarro, F., Glazovsky, A., Vasilenko, E., Lapazaran, J., Głowacki, P., Migała, K., Bałut, A. & Piwowar, B. (2005). Temporal changes in the radiophysical properties of a polythermal glacier in Spitsbergen. *Annals of Glaciology, 42*(1), 125-134. DOI: 10.3189/172756405781812754

Jansson, P., Hock, R. & Schneider, T. (2003) The Concept of Glacier Storage: a Review. *Journal of Hydrology, 282*, 116-129. DOI: 10.1016/S0022-1694(03)00258-0

Japan Aerospace Exploration Agency (2016) *PALSAR-2 Level 1.1/2.1/1.5/3.1 CEOS SAR Product Format Description*. Retrieved from the Earth Observation Research Center, Japan Aerospace Exploration Agency website: https://www.eorc.jaxa.jp/ALOS-2/en/doc/fdata/PALSAR-2_xx_Format_CEOS_E_e.pdf

Jenks, G.F. & Caspall, F.C. (1971) Error on Choroplethic Maps: Definition, Measurement, Reduction. *Annals of the Association of American Geographers, 61*(2), 217-244. DOI: 10.1111/j.1467-8306.1971.tb00779.x

Jones, E., Caprarelli, G., Mills, F.P., Doran, B. & Clarke, J. (2014) An Alternative Approach to Mapping Thermophysical Units from Martian Thermal Inertia and Albedo Data Using a Combination of Unsupervised Classification Techniques. *Remote Sensing, 6*, 5184-5237. DOI: 10.3390/rs6065184

König, M., Wadham, J., Winther, J., Kohler, J. & Nuttall, A. (2002). Detection of superimposed ice on the glaciers Kongsvegen and midre Lovénbreen, Svalbard, using SAR satellite imagery. *Annals of Glaciology, 34*, 335-342. DOI: 10.3189/172756402781817617

König, M., Winther, J., Kohler, J. & König, F. (2004). Two methods for firn-area and mass-balance monitoring of Svalbard glaciers with SAR satellite images. *Journal of Glaciology, 50*(168), 116-128. DOI: 10.3189/172756504781830286

Kult, A. (2012) *Volume 8: ASAR Products Specifications.* (Report No. PO-RS-MDA-GS-2009). Retrieved from the European Space Agency: Sensor Performance, Products and

Algorithms website: https://earth.esa.int/web/sppa/mission-performance/esa-missions/envisat#product_spec

MacDonald, Dettwiler and Associates Ltd. (2016) *RADARSAT-2 Product Format Definition* (Report No. RN-RP-51-2713). Richmond, B.C.: MacDonald, Dettwiler and Associates Ltd.

Matsuoka, K., Thorsteinsson, T., Björnsson, H., & Waddington, E. (2007). Anisotropic radio-wave scattering from englacial water regimes, Mýrdalsjökull, Iceland. *Journal of Glaciology, 53*(182), 473-478. DOI: 10.3189/002214307783258422

Maxar Technologies Ltd. (2018) *RADARSAT-2 Product Description* (Report No. RN-SP-52-1238). Richmond, B.C.: Maxar Technologies Ltd.

Miranda, N., Meadows, P.J. (2015) *Radiometric Calibration of S-1 Level-1 Products Generated by the S-1 IPF* (Report No. ESA-EOPG-CSCOP-TN-0002). Retrieved from the European Space Agency: Sentinel Online website: https://sentinel.esa.int/documents/247904/685163/S1-Radiometric-Calibration-V1.0.pdf

Moholdt, G., Nuth, C., Hagen, J. O. & Kohler, J. (2010) Recent elevation changes of Svalbard glaciers derived from ICESat laser altimetry. *Remote Sensing of Environment, 114*(11), 2756-2767. DOI: 10.1016/j.rse.2010.06.008

Müller, F. (1962) Zonation in the Accumulation Area of the Glaciers of Axel Heiberg Island, N.W.T., Canada. *Journal of Glaciology,* 4, 302-311. DOI: 10.3189/S0022143000027623

Navarro, F. J., Macheret, Y. Y. & Benjumea, B. (2005). Application of radar and seismic methods for the investigation of temperate glaciers. *Journal of Applied Geophysics, 57*(3), 193–211. DOI: 10.1016/j.jappgeo.2004.11.002

Nordli, Ø., Przybylak, R., Ogilvie, A. E. J. & Isaksen, K. (2014) Long-term temperature trends and variability on Spitsbergen: the extended Svalbard Airport temperature series, 1898–2012, *Polar Research,* 33(1), 21349, DOI: 10.3402/polar.v33.21349

Nuth, C., Moholdt, G., Kohler, J., Hagen, J. O. & Kääb, A. (2010), Svalbard glacier elevation changes and contribution to sea level rise. *Journal of Geophysical Reearch, 115*(F01008). DOI: 10.1029/2008JF001223.

Nuth, C., Kohler, J., König, M., von Deschwanden, A., Hagen, J. O., Kääb, A., Moholdt, G. & Pettersson, R. (2013) Decadal changes from a multi-temporal glacier inventory of Svalbard. *The Cryosphere, 7*, 1603–1621, DOI: 10.5194/tc-7-1603-2013

Langley, K., Hamran, S. E., Hogda, K. A., Storvold, R., Brandt, O., Hagen, J. O., & Kohler, J. (2007) Use of C-Band Ground Penetrating Radar to Determine Backscatter Sources Within Glaciers. *IEEE Transactions on Geoscience and Remote Sensing, 45*(5), 1236-1246. DOI: 10.1109/TGRS.2007.892600

Langley, K., Hamran, S.E., Hogda, K.A., Storvold, R., Brandt, O., Kohler, J., Hagen, J.O. (2008) From glacier facies to SAR backscatter zones via GPR. *IEEE Transactions on Geoscience and Remote Sensing, 46*(9), 2506–2516. DOI: 10.1109/TGRS.2008.918648.

Laska, M., Barzycka, B., & Luks, B. (2017a). Melting characteristics of snow cover on tidewater glaciers in Hornsund fjord, Svalbard. *Water, 9*(10), 804. DOI: 10.3390/w9100804

Laska, M., Grabiec, M., Ignatiuk, D., & Budzik, T. (2017b). Snow deposition patterns on southern Spitsbergen glaciers, Svalbard, in relation to recent meteorological conditions and local topography. *Geografiska Annaler: Series A, Physical Geography, 99*(3), 262-287. DOI: 10.1080/04353676.2017.1327321

Lee, J. S., Grunes, M. R., Ainsworth, T. L., Du, L. J., Schuler, D. L. & Cloude, S. R. (1999) Unsupervised classification using polarimetric decomposition and the complex Wishart classifier. *IEEE Transactions on Geoscience and Remote Sensing, 37*(5), 2249-2258. DOI: 10.1109/36.789621

Lee, J. S. & Pottier, E. (2009) Polarimetric SAR Speckle Filtering. In: *Polarimetric Radar Imaging: From Basics to Applications* (pp. 143-178) Boca Raton, FL: CRC Press.

Lee, J. S., Wen, J. H., Ainsworth, T. L., Chen, K. S. & Chen, A. J. (2009) Improved Sigma Filter for Speckle Filtering of SAR Imagery. *IEEE Transactions on Geoscience and Remote Sensing, 47*(1), 202-213. DOI: 10.1109/TGRS.2008.2002881

Lillesand, T., Kiefer, R.W., Chipman, J. (2008) *Remote Sensing and Image Interpretation, 6th Edition.* pp. 554-557, 568-572, 585-592. Hoboken, NJ: John Wiley & Sons. ISBN 978-0-470-05245-7

Łupikasza, E.B., Ignatiuk, D., Grabiec, M., Cielecka-Nowak, K., Laska, M., Jania, J., Luks, B., Uszczyk, A. & Budzik, T. (2019) The Role of Winter Rain in the Glacial System on Svalbard. *Water, 11*, 334. DOI: 10.3390/w11020334

Østby, T. I., Schuler, T. V., Hagen, J. O., Hock, R., Kohler, J., & Reijmer, C. H. (2017) Diagnosing the decline in climatic mass balance of glaciers in Svalbard over 1957–2014. *The Cryosphere, 11*, 191–215. DOI: 10.5194/tc-11-191-2017

Pattyn, F., Delcourt, C., Samyn, D., De Smedt, B., & Nolan, M. (2009). Bed properties and hydrological conditions underneath McCall Glacier, Alaska, USA. *Annals of Glaciology, 50*(51), 80-84. DOI: 10.3189/172756409789097559

Peter, H., Jäggi, A., Fernández, J., Escobar, D., Ayuga, F., Arnold, D., Wermuth, M., Hackel, S., Otten, M., Simons, W., Visser, P., Hugentobler, U. & Féménias, P. (2017) Sentinel-1A - First precise orbit determination results. *Advances in Space Research, 60*(1), 879-892. DOI: 10.1016/j.asr.2017.05.034

Pope, A. & Rees, G. (2014) Using in situ spectra to explore Landsat classification of glacier surfaces. *International Journal of Applied Earth Observation and Geoinformation*, *27*(A), 42-52. DOI: 10.1016/j.jag.2013.08.007

Porter, C., Morin, P., Howat, I., Noh, M-J., Bates, B., Peterman, K., Keesey, S., Schlenk, M., Gardiner, J., Tomko, K., Willis, M., Kelleher, C., Cloutier, M., Husby, E., Foga, S., Nakamura, H., Platson, M., Wethington, M. Jr., Williamson, C., Bauer, G., Enos, J., Arnold, G., Kramer, W., Becker, P., Doshi, A., D’Souza, C., Cummens, P., Laurier, F. & Bojesen, M. (2018) *ArcticDEM*, Harvard Dataverse, V1, [2018] DOI: 10.7910/DVN/OHHUKH

Pottier, E. & Ferro-Famil, L. (2012) PolSARPro V5.0: An ESA educational toolbox used for self-education in the field of POLSAR and POL-INSAR data analysis (pp. 7377–7380). In *Proceedings of the IEEE Geoscience and Remote Sensing Symposium (IGARSS), 22–27 July 2012, Munich, Germany*. Institute of Electrical and Electronics Engineeers, Piscataway, NJ. DOI: 10.1109/IGARSS.2012.6351925

Rignot, E., Echelmeyer, K. & Krabill, W. (2001). Penetration Depth of Interferometric Synthetic- Aperture Radar Signals in Snow and Ice. *Geophysical Research Letters, 28*, 3501-3504. DOI: 10.1029/2000GL012484

Rosich, B. & Meadows, P. (2004) *Absolute Calibration of ASAR Level 1 Products Generated with PF-ASAR.* (Report No. ENVI-CLVL-EOPG-TN-03-0010). Frascati (Rome): ESRIN European Space Agency.

Rott, H., & Mätzler, C. (1987). Possibilities and Limits of Synthetic Aperture Radar for Snow and Glacier Surveying. *Annals of Glaciology, 9*, 195-199. DOI: 10.3189/S0260305500000604

Serreze, M.C. & Francis, J.A. (2006) The Arctic Amplification Debate. *Climatic Change 76*, 241–264. DOI: 10.1007/s10584-005-9017-y

Shimada, M., Isoguchi, O., Tadono, T. & Isono, K. (2009) PALSAR Radiometric and Geometric Calibration. *IEEE Transactions on Geoscience and Remote Sensing, 47*(12), 3915-3932. DOI: 10.1109/TGRS.2009.2023909

Small, D. & Shubert, A. (2008) *Guide to ASAR Geocoding.* (Report No. RSL-ASAR-GC-AD) Retrieved from the European Space Agency: NEST website: https://earth.esa.int/web/nest/documents/references

Small, D. & Shubert, A. (2019) *Guide to Sentinel-1 Geocoding.* (Report No. UZH-S1-GC-AD) Retrieved from the European Space Agency: Sentinel Online website: https://sentinel.esa.int/documents/247904/1653442/Guide-to-Sentinel-1-Geocoding.pdf

Sulebak, J.R., Etzelmüller, B. & Sollid, J.L. (1997) Landscape regionalization by automatic classification of landform elements. *Norsk Geografisk Tidsskrift - Norwegian Journal of Geography, 51*(1), 35-45. DOI: 10.1080/00291959708552362

Szafraniec, E. (2018) Deglaciation rate on southern and western Spitsbergen in the conditions of Arctic amplification. *Polish Polar Research, 39*(1), 77-98. DOI: 10.24425/118739

Tebaldini, S., Nagler, T., Rott, H. & Heilig, A. (2016) Imaging the Internal Structure of an Alpine Glacier via L-Band Airborne SAR Tomography. *IEEE Transactions on Geoscience and Remote Sensing, 54*(12), 7197-7209. DOI: 10.1109/TGRS.2016.2597361

Townsend, P. A., Lookingbill, T. R., Kingdon, C. C. & Gardner, R. H. (2009) Spatial pattern analysis for monitoring protected areas. *Remote Sensing of Environment, 113*(7), 1410-1420. DOI: 10.1016/j.rse.2008.05.023

Uszczyk, A., Grabiec, M., Laska, M., Kuhn, M. & Ignatiuk, D. (2019) Importance of Snow as Component of Surface Mass Balance of Arctic Glacier (Hansbreen, Southern Spitsbergen). *Polish Polar Research, 40*(4), 311-338. DOI: 10.24425/ppr.2019.130901

van Pelt, W., Pohjola, V., Pettersson, R., Marchenko, S., Kohler, J., Luks, B., Hagen, J. O., Schuler, T. V., Dunse, T., Noël, B. & Reijmer, C. (2019). A long-term dataset of climatic mass balance, snow conditions, and runoff in Svalbard (1957–2018). *The Cryosphere, 13*, 2259–2280. DOI: 10.5194/tc-13-2259-2019

Vikhamar-Schuler D., Førland, E. J., Lutz, J. & Gjelten, H. M. (2019). *Evaluation of downscaled reanalysis and observations for Svalbard. Background report for Climate in*

Svalbard 2100 (Report No. NCCS 4/2019) Retrieved from the Norwegian Centre for Climate Services website: www.klimaservicesenter.no

Vincent, P., Bourbiguot, M., Johnsen, H. & Piantanida, R. (2019) *Sentinel-1 Product Specification* (Report No. S1-RS-MDA-52-7441). Retrieved from the European Space Agency: Sentinel Online website: https://sentinel.esa.int/documents/247904/349449/Sentinel-1-Product-Specification.pdf

WGMS (2019): Fluctuations of Glaciers Database. World Glacier Monitoring Service, Zurich, Switzerland. DOI: 10.5904/wgms-fog-2019-12.

Woodward, J., Sharp, M. & Arendt, A. (1997). The influence of superimposed-ice formation on the sensitivity of glacier mass balance to climate change. *Annals of Glaciology, 24*, 186-190. DOI: 10.3189/S0260305500012155